Interplay of rare earth and iron magnetism in *R*FeAsO (*R*=La, Ce, Pr, and Sm): Muon-spin relaxation study and symmetry analysis

H. Maeter,[1] H. Luetkens,[2] Yu. G. Pashkevich,[3] A. Kwadrin,[1] R. Khasanov,[2] A. Amato,[2] A. A. Gusev,[3] K. V. Lamonova,[3] D. A. Chervinskii,[3] R. Klingeler,[4] C. Hess,[4] G. Behr,[4] B. Büchner,[4] and H.-H. Klauss[1,*]

[1]*Institut für Festkörperphysik, TU Dresden, D-01069 Dresden, Germany*

[2]*Laboratory for Muon-Spin Spectroscopy, Paul Scherrer Institut, CH-5232 Villigen PSI, Switzerland*

[3]*A. A. Galkin Donetsk Phystech NASU, 83114 Donetsk, Ukraine*

[4]*Leibniz-Institut für Festkörper- und Werkstoffforschung (IFW) Dresden, D-01171 Dresden, Germany*

(Received 17 April 2009; revised manuscript received 21 August 2009; published 25 September 2009)

We report zero-field muon spin relaxation (μSR) measurements on *R*FeAsO with *R*=La, Ce, Pr, and Sm. We study the interaction of the FeAs and *R* (rare-earth) electronic systems in the nonsuperconducting magnetically ordered parent compounds of $RFeAsO_{1-x}F_x$ superconductors via a detailed comparison of the local hyperfine fields at the muon site with available Mössbauer spectroscopy and neutron-scattering data. These studies provide microscopic evidence of long-range commensurate magnetic Fe order with the Fe moments not varying by more than 15% within the series *R*FeAsO with *R*=La, Ce, Pr, and Sm. At low temperatures, long-range *R* magnetic order is also observed. Different combined Fe and *R* magnetic structures are proposed for all compounds using the muon site in the crystal structure obtained by electronic potential calculations. Our data point to a strong effect of *R* order on the iron subsystem in the case of different symmetry of Fe and *R* order parameters resulting in a Fe spin reorientation in the *R*-ordered phase in PrFeAsO. Our symmetry analysis proves the absence of collinear Fe-*R* Heisenberg interactions in *R*FeAsO. A strong Fe-Ce coupling due to non-Heisenberg anisotropic exchange is found in CeFeAsO which results in a large staggered Ce magnetization induced by the magnetically ordered Fe sublattice far above T_N^{Ce}. Finally, we argue that the magnetic *R*-Fe interaction is probably not crucial for the observed enhanced superconductivity in $RFeAsO_{1-x}F_x$ with a magnetic *R* ion.

DOI: 10.1103/PhysRevB.80.094524 PACS number(s): 75.30.Fv, 74.70.−b, 76.75.+i, 76.80.+y

I. INTRODUCTION

The recent discovery of high-temperature superconductivity in $LaFeAsO_{1-x}F_x$ by Kamihara and co-workers has triggered intense research in the Fe pnictides.[1] In its wake, superconductivity with transition temperatures that exceed 50 K has been found in the oxopnictide materials in which La is substituted by *R*=Sm, Ce, Nd, Pr, and Gd, respectively.[2–6] Besides the high critical temperatures, striking similarities to the properties of the high-T_c cuprates have been pointed out. As with the cuprates, the Fe pnictides have a layered crystal structure with alternating FeAs and *R*O sheets, where the Fe ions are arranged on a simple square lattice.[1] Superconductivity emerges in the pnictides when doping the antiferromagnetic parent compound either with electrons or holes which suppresses the magnetic order.[14,18] These similarities raised the hope that cuprates and pnictides share a common mechanism for superconductivity and that after 20 year of research on high-T_c cuprates, the Fe pnictides may provide insight into the superconducting coupling mechanism and verify existing theories about high-temperature superconductivity.

In contrast to the cuprates, the nonsuperconducting magnetic parent compound is not a Mott-Hubbard insulator but a metal. Theoretical studies reveal a two-dimensional electronic structure with all Fe 3*d* bands contributing to the density of states at the Fermi level.[7] Neutron diffraction[13] and local probe techniques such as Mössbauer spectroscopy and μSR (Refs. 12, 39, and 40) prove that the *R*FeAsO parent compounds order in a commensurate spin-density wave (SDW) magnetic order with a strongly reduced ordered Fe moment. Neutron studies suggest a columnar magnetic structure with a Fe magnetic moment between $0.25\mu_B$ and $0.8\mu_B$ below $T_N \approx 140$ K that depends on *R*.[43] Due to the small size of the ordered SDW moment (compared to metallic iron with a moment of approximately $2.2\mu_B$ per Fe) and the lack of large single crystals, the temperature dependence of the magnetic order parameter can be determined by local probe techniques with a much higher accuracy than with neutron scattering.[12] Note that the magnetic transition in the *R*FeAsO system is always preceded by an orthorhombic structural distortion which appears at T_S, which is about 10–20 K above T_N.

It is still an open question why the rare-earth-containing systems in the series $RFeAsO_{1-x}F_x$ with a localized *R* magnetic moment have a higher T_c than $LaFeAsO_{1-x}F_x$. One suggestion is based on a purely geometrical argument. It is argued that the different ionic radii of the rare-earth elements change the Fe-As-Fe bond angles in the Fe-As plane and the FeAs-FeAs interplane distance. As a consequence, the planar anisotropy of the electronic properties may be better for superconductivity in case of *R*=Ce,Pr,Nd, etc. On the other hand, the electronic interaction of the *R* 4*f* electrons with the Fe conduction band states may be crucial to enhance the density of states at the Fermi energy.

In this work, we examine the interaction of the FeAs electronic bands with the rare-earth subsystem by a detailed comparison of the local hyperfine fields at the muon site and Fe nucleus to neutron-scattering results. These studies were performed on the undoped magnetically ordered parent com-

pounds of the RFeAsO$_{1-x}$F$_x$ superconductors. We report zero-field (ZF) muon spin relaxation measurements on powder samples of RFeAsO with R=La, Ce, Pr, and Sm. We provide microscopic evidence of static commensurate magnetic order of Fe moments. The Néel temperatures and the temperature dependence of the Fe sublattice magnetization were determined with high precision and are compared to available Mössbauer spectroscopy and neutron-scattering results from the literature. In contrast to neutron studies, our measurements prove that the size of the ordered Fe moment is independent of the rare-earth ion. For a quantitative analysis of the μSR spectra, the muon site in the RFeAsO crystal structure has been determined by electronic potential calculations using a modified Thomas-Fermi approach. Spontaneous magnetic ordering of the rare-earth magnetic moment is observed by μSR below T_N^R=4.4(3), 11(1), and 4.66(5) K for R=Ce, Pr, and Sm, respectively. Iron and R magnetic structures are proposed for all compounds on the basis of a detailed symmetry analysis and magnetic-dipole field calculations at the muon site on the one hand and μSR, Mössbauer spectroscopy, and neutron-scattering data on the other. Noncollinear magnetic order of Ce and Sm is found in the corresponding compounds, which we explain by a weak coupling of adjacent R planes in the R-O-R layer. In PrFeAsO, the μSR data suggest an Fe spin reorientation developing below T_N^{Pr}, while the Fe order is unaltered below T_N^R in the Sm and Ce compounds.

In CeFeAsO, we find a sizable staggered magnetization of the Ce ions induced by the Fe subsystem already far above T_N^{Ce} which amounts to approximately $0.3\mu_B$ near to T_N^{Ce}. We argue that the neglect of the Ce magnetization may have caused the overestimation of the ordered Fe moment in recent neutron-diffraction studies. Our symmetry analysis proves the absence of collinear Fe-R Heisenberg interaction in RFeAsO compounds. Using classical and quantum-mechanical approaches, we deduce Fe-Ce and Ce-Ce exchange coupling constants and show that the Fe-Ce non-Heisenberg exchange interaction is exceptionally strong and of the same order as the Ce-Ce exchange interaction. In the Sm and Pr compounds, the observed coupling between the R and the Fe subsystems is found to be much weaker than in CeFeAsO. Therefore, we conclude that the magnetic R-Fe interaction is probably not crucial for the enhanced superconducting transition temperatures in RFeAsO$_{1-x}$F$_x$ with magnetic 4f ions compared to LaFeAsO$_{1-x}$F$_x$, since only in CeFeAsO a strong R-Fe coupling is observed.

II. EXPERIMENTAL

Polycrystalline RFeAsO has been prepared by using a two-step solid-state reaction method, similar to that described by Zhu *et al.*, and annealed in vacuum.[8] The crystal structure and the composition were investigated by powder x-ray diffraction. From the x-ray diffraction data, no impurity phases are inferred.

In a μSR experiment, nearly 100% spin-polarized muons are implanted into the sample one at a time. The positively charged μ^+ thermalize at interstitial lattice sites, where they act as magnetic microprobes. In a magnetic material, the muon spin precesses about the local magnetic field B at the muon site with the Larmor frequency $f_\mu=\gamma_\mu/(2\pi)B$ (muon gyromagnetic ratio $\gamma_\mu/2\pi$=135.5 MHz T^{-1}). With a lifetime of τ_μ=2.2 μs, the muon decays into two neutrinos and a positron, the latter being predominantly emitted along the direction of the muon spin at the moment of the decay. Measurement of both the direction of positron emission as well as the time between muon implantation and positron detection for an ensemble of several millions of muons provides the time evolution of the muon spin polarization $P(t)$ along the initial muon spin direction. Magnetic materials with commensurate order possess a well-defined local field B at the muon site. Therefore, a coherent muon spin precession can be observed, which for powder samples has the following functional form (see, e.g., Ref. 9):

$$P(t)=\sum_{i=1}^{n} P_i\left[\frac{2}{3}e^{-\lambda_T^i t}\cos(\gamma_\mu B_i t+\phi)+\frac{1}{3}e^{-\lambda_L^i t}\right]. \qquad (1)$$

The occurrence of 2/3 oscillating and 1/3 nonoscillating μSR signal fractions originates from the spatial averaging in powder samples where 2/3 of the magnetic field components are perpendicular to the μ^+ spin and cause a precession, while the 1/3 longitudinal field components do not. The relaxation of the oscillation, λ_T, is a measure of the width of the static field distribution $\Delta B=\lambda_T/\gamma_\mu$. Dynamical effects are also present in λ_T while the relaxation of the second term, λ_L, is due to dynamic magnetic fluctuations only.

If n magnetically inequivalent muon sites exist in the crystallographic or magnetic structure, each of the sites contributes to the μSR signal with its weight P_i. In 100% magnetically ordered specimens, ΣP_i=1. Therefore, μSR not only provides a highly sensitive measure of the magnetic order parameter via internal magnetic fields B, but also allows to independently determine the magnetic volume fraction. This is not possible with nonlocal probes such as, e.g., neutron diffraction.

III. MUON SPIN RELAXATION RESULTS

In Fig. 1, ZF μSR time spectra are shown for RFeAsO with R=La, Ce, Pr, and Sm. At high temperatures above 150 K, no muon spin precession and only a very weak depolarization of the μ^+ polarization $P(t)$ is observed. This weak depolarization and its Gaussian shape are typical for a paramagnetic material and reflect the occurrence of a small Gaussian-Kubo-Toyabe depolarization originating from the interaction of the μ^+ spin with randomly oriented nuclear magnetic moments.[19] At temperatures below T_N a well-defined spontaneous muon spin precession is observed in all compounds indicating a well-defined magnetic field at the muon sites. Therefore, long-range static magnetic order with a commensurate magnetic structure is realized in all investigated compounds of the RFeAsO series. Accordingly, incommensurate order or spin-glass magnetism can be excluded. Only in LaFeAsO, a second μSR frequency with lower amplitude $P_2\approx 0.30$ is observed in addition to the main precession signal $P_1\approx 0.70$. As described above, this indicates that two magnetically inequivalent muon stopping sites are

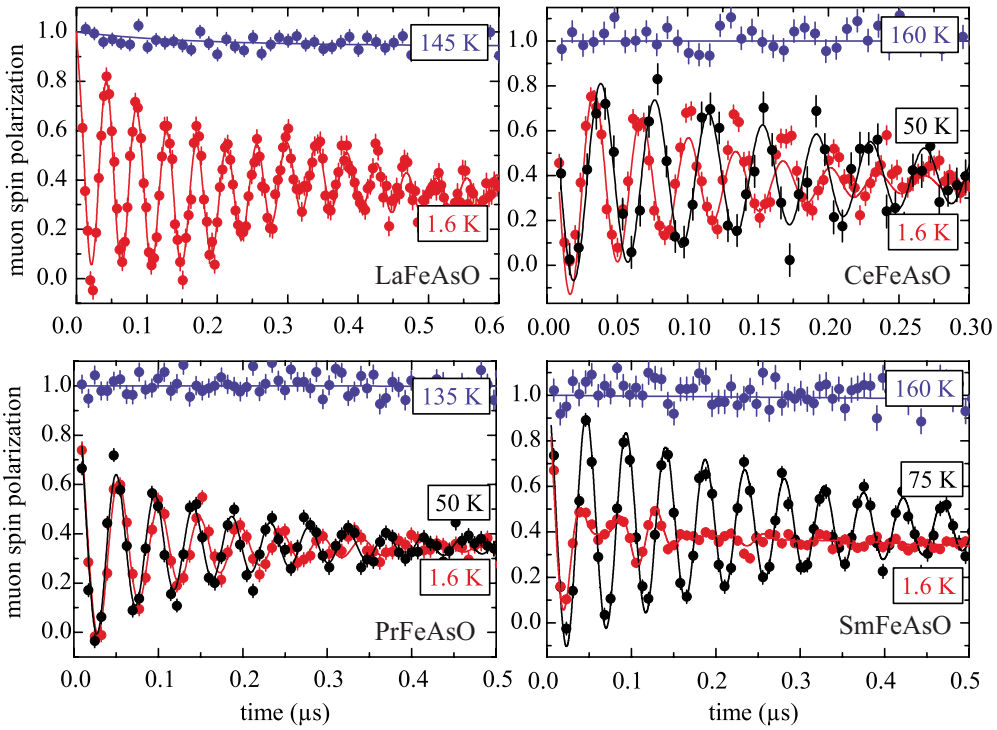

FIG. 1. (Color online) Zero-field μSR spectra for RFeAsO with R=La, Ce, Pr, and Sm for three different temperatures $T>T_N$, $T_N>T>T_N^R$, and $T<T_N^R$.

present in the crystal lattice or magnetic structure. The (static) magnetic order develops in the full sample volume below T_N as evidenced by the magnetic μSR signal fraction shown in the inset of Fig. 2. The observed 5–10 % residual nonmagnetic signal fractions observed in our measurements are due to muons that do not hit the sample but stop in the sample holder or cryostat walls.

The Néel temperatures obtained from the μSR measurements (superscript μ) are summarized in Table I. As we have shown previously for LaFeAsO, the Néel temperature T_N of the iron subsystem and the structural transition temperature T_S can also be determined from anomalies in the temperature dependence of the resistivity.[12] For all RFeAsO compounds

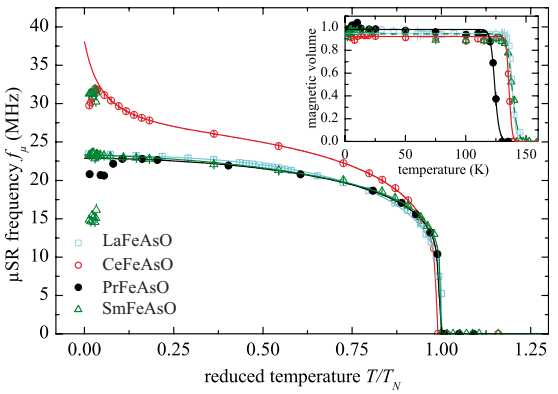

FIG. 2. (Color online) Muon-spin precession frequency as a function of reduced temperature for RFeAsO with R=La, Ce, Pr, and Sm. Inset: Magnetic signal fraction for RFeAsO, with R=La, Ce, Pr, and Sm. Lines are guides to the eyes.

investigated here, pronounced anomalies have been observed.[10–12,15] The corresponding transition temperatures T_N^o and T_S^o are listed also in Table I. In addition, magnetic T_N^n of the iron and the rare-earth (superscript R) subsystems and structural, $T_S^{n/x}$, transition temperatures deduced from neutron (superscript n) and x-ray scattering (superscript x) experiments are given for comparison. Note that for SmFeAsO, no neutron data are available due to the high neutron absorption of natural Sm.

Within the experimental error, the Néel temperatures determined from μSR, resistivity, and neutron scattering agree very well. The structural transition is found to be clearly separated by 10–20 K from T_N for all investigated compounds. Our highly sensitive μSR investigations prove the absence of static long-range magnetic order between T_N and T_S. Also, no static magnetic short-range correlation or disordered magnetism, which would have been easily detected by μSR, has been observed. However, our μSR data do not rule out a dynamic nematic magnetic phase with broken Ising symmetry that has recently been proposed to develop below T_S,[20,21] provided that the fluctuations are faster than approximately 10 GHz.

A. Iron magnetic order

Now we turn our discussion to the temperature dependence of the Fe sublattice magnetization. We will first concentrate on the temperature regime above the static order of the rare-earth moment. The temperature dependence of the muon spin precession frequency for RFeAsO with R=La, Ce, Pr, and Sm is shown in Fig. 2 for comparison. All compounds display a very similar temperature dependence and

TABLE I. Magnetic and structural transition temperatures of *R*FeAsO with *R*=La, Pr, Sm, and Ce. In the cases where no reference is given, the transition temperatures were measured exactly on the samples used in this study (Refs. 10–12, 14, and 15). All temperatures are given in K. See text for the abbreviations in the superscripts.

R	$T_N^{\mu,R}$	$T_N^{n,R}$	T_N^{μ}	T_N^{n}	T_N^{o}	$T_S^{n/x}$	T_S^{o}
La			139(1)	137(3)[a]	138.0	158(3)	156.0
Ce	4.4(3)	≈5 [b]	137(2)	139(5)[b]	134.8	152.2	151.5
Pr	11(1)	11	123(2)	127.0[c]	127.0	136.0	136.0
Sm	4.66(5)		138(2)		136.5	158.5	160.0

[a]Reference 13.
[b]Reference 16.
[c]Reference 17.

absolute value of the μSR frequency. Only the R=Ce compound shows a higher frequency and a stronger temperature dependence below T_N. In Fig. 3, the μSR frequency $f_\mu(T)$ is shown together with the average magnetic hyperfine field $B_{hf}(T)$ at the Fe site from ^{57}Fe Mössbauer spectroscopy[23] and the square root of the magnetic Bragg-peak intensity $\sqrt{I(T)}$ of available neutron-scattering data.[16,17,22] The scale for $f_\mu(T)$ and $B_{hf}(T)$ is the same for all diagrams and the scales for $\sqrt{I(T)}$ have been adjusted so that the μSR and neutron data coincide as much as possible. In the following, we discuss the data for each compound separately.

1. LaFeAsO

In LaFeAsO, all three observables $f_\mu(T)$, $B_{hf}(T)$, and $\sqrt{I(T)}$ scale with each other since they all measure the size of the ordered Fe moment. A gradual increase of the ordered Fe moment observed below T_N indicates a second-order phase transition. The steep increase of the order parameter deviates from the mean-field $\sqrt{1-(T/T_N)^2}$ temperature dependence. As we have shown previously, this can be understood qualitatively in the framework of a four-band spin-density model.[12] The onset of the magnetic order is accompanied by a broad static magnetic field distribution $\Delta B=\lambda_T/\gamma_\mu$ at the

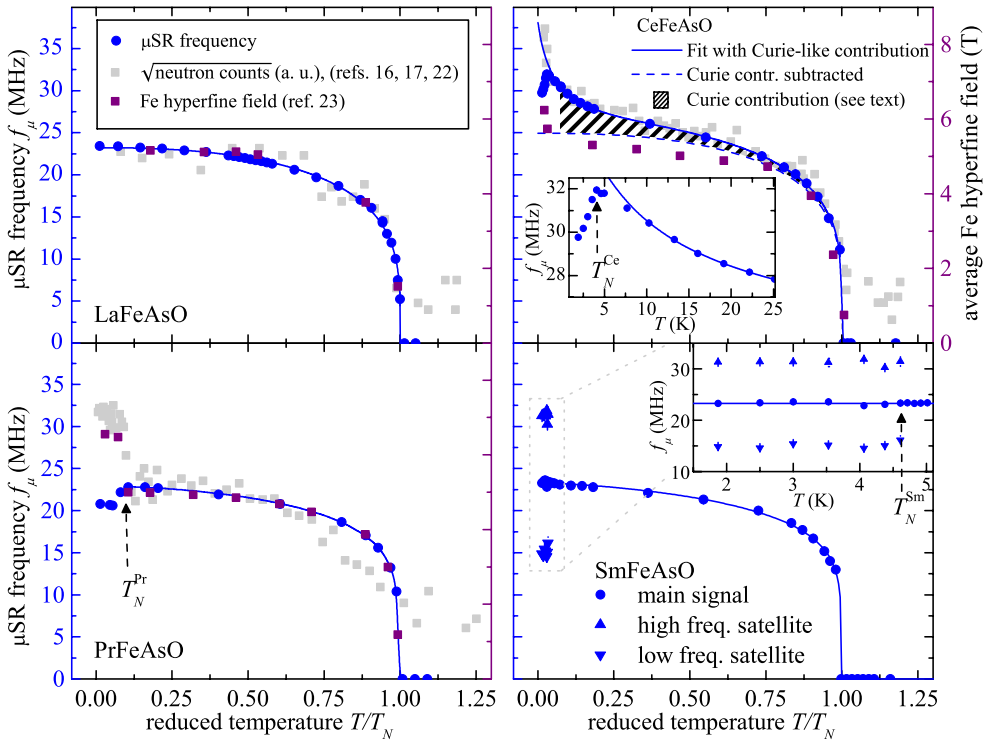

FIG. 3. (Color online) Main μSR frequency as a function of reduced temperature T/T_N^{Fe} together with the average magnetic hyperfine field at the Fe site from Mössbauer spectroscopy (Ref. 23) and the square root of the magnetic Bragg-peak intensity of available neutron-scattering (Refs. 16, 17, and 22) data. Note that the scales of $f_{\mu SR}$ and of B_{hf} are the same in all graphs. Some axes' labels have been omitted for clarity. Typically, error bars of the μSR frequency are smaller than the data points.

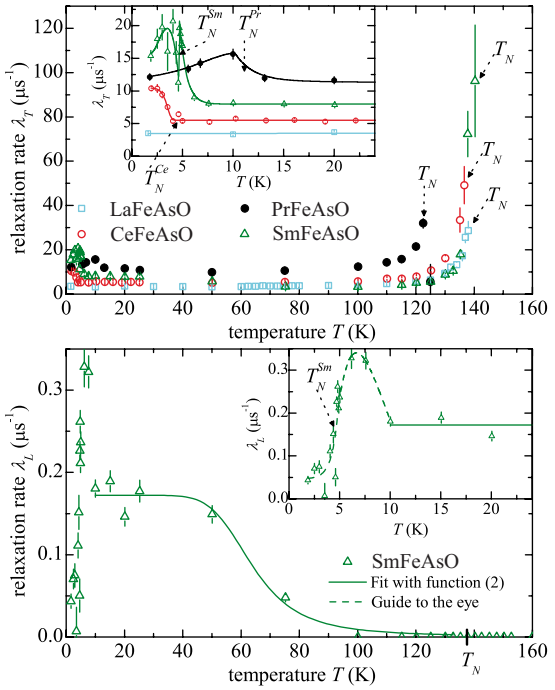

FIG. 4. (Color online) (Top) Transverse relaxation rate $\lambda_T(T)$ for RFeAsO, with R=La, Ce, Pr, and Sm. Lines are guides to the eyes. (Bottom) Longitudinal relaxation rate $\lambda_L(T)$ for RFeAsO with R =Sm only. Solid line is a fit of Eq. (2) to the data. Dashed line is a guide to the eyes.

muon site (see Sec. II) that narrows rapidly with decreasing temperature, as can be seen in Fig. 4(a). The relative width of the field distribution $\Delta_{rel}=\Delta B/B$ is proportional to $(T-T_N^{\mathrm{Fe}})^{-1}$, i.e., Δ_{rel} diverges with T^{-1} as the temperature approaches the Néel temperature of the Fe sublattice from below for all systems presented here (not shown). Except for SmFeAsO, no dynamic magnetic fluctuations are detected ($\lambda_L=0$) for temperatures below T_N^{Fe}.

2. SmFeAsO

For SmFeAsO, no neutron and Mössbauer data are available. Qualitatively and quantitatively, the temperature dependence of the observed μSR frequency is very similar to that of LaFeAsO and consistent with previously reported μSR data.[41] A sharp increase of the ordered Fe moment is observed below T_N^{Fe}. Also, the saturation value of $f_0 \approx 23$ MHz indicates the same size of the ordered Fe moment in LaFeAsO and SmFeAsO assuming the same hyperfine coupling constants in these isostructural compounds. In contrast to the other systems, magnetic fluctuations in the time window of μSR are detected in this system that cause the dynamic relaxation rate λ_L to increase gradually and to saturate between 10 and 30 K. As reported by Khasanov *et al.*, this can be associated with fluctuating Sm magnetic moments due to a thermally activated population of Sm crystal electric field levels.[28] The temperature dependence of the dynamic relaxation rate is well described by

$$\frac{1}{\lambda_L(T)} = \frac{1}{\lambda_L^0} + \frac{1}{C\exp(E_0/k_BT)}, \tag{2}$$

with a saturation value λ_L^0 at low temperatures and an activation energy E_0 that is related to low-lying Sm crystal electric field levels. The rough agreement of the activation energy E_0 of the Sm magnetic moment fluctuations with the Sm crystal electric field splitting has been confirmed by specific-heat measurements reported by Baker and co-workers.[54] A fit of Eq. (2) to the longitudinal relaxation rate $\lambda_L(T)$ is shown in Fig. 4 and yields λ_L^0=0.172(6) μs^{-1}, C=0.001 μs^{-1}, and E_0=44(10) meV. This value for E_0 is approximately 2 times higher than in the oxygen deficient $SmFeAsO_{0.75}$ studied by Khasanov *et al.*[28] However, one has to take into account that the oxygen deficiency in $SmFeAsO_{0.75}$ causes a higher defect density and changes of the lattice parameters.[29] Therefore, a different activation energy E_0 for the undoped SmFeAsO compared to $SmFeAsO_{0.75}$ is possible.

3. PrFeAsO

Apart from a slightly reduced Néel temperature, PrFeAsO shows the same temperature dependence and saturation value of the Fe sublattice magnetization, i.e., $f_\mu(T)$ as SmFeAsO. Note that again the saturation values for f_μ and B_{hf} are very similar to that of LaFeAsO, indicating the same size of the ordered Fe moment. A close comparison of $f_\mu(T)$ and $B_{hf}(T)$ reveals that $f_\mu(T)$ is systematically reduced by a small amount compared to $B_{hf}(T)$. This phenomenon can be explained by the same mechanism found in the Ce system (see below and Sec. VI). In the case of PrFeAsO, the muon spin-polarization function (1) did not approximate the data very well and a nonzero phase ϕ of the oscillation and a generalized exponential relaxation function $\exp[-(\lambda_T t)^\alpha]$ had to be used to describe the data.

4. CeFeAsO

A qualitatively different behavior is observed for the CeFeAsO compound. Neutron diffraction as well as μSR data do not scale with the observed hyperfine field B_{hf} at the Fe site. The magnetic Bragg intensity as well as the internal magnetic field at the muon site measured by the muon precession frequency continuously increase below T_N. Only the Mössbauer hyperfine field displays the same rapid saturation below T_N with the same ordered moment as observed for the La and Pr compounds.[23] Therefore, we conclude that the μSR as well as the neutron data do not solely measure the Fe sublattice magnetization, but also contain a significant contribution from the Ce sublattice. The ^{57}Fe Mössbauer spectroscopy provides the most accurate measurement of the on-site Fe sublattice magnetization without sizable contribution from the rare-earth moments due to a weak transferred hyperfine coupling. In contrast, a magnetization on the rare-earth site induced by the Fe subsystem has the same symmetry as the Fe order and therefore contributes to the same Bragg peaks. In principle, neutron scattering can distinguish between the different contributions from the Fe and the Ce sublattices by fitting the different magnetic form factors. This has not been done for $T > T_N^R$ in the neutron studies[16,17,22]

shown in Fig. 3, where the whole magnetic intensity has been attributed to originate from Fe moments alone. Similar to the neutron data, the local field at the muon site also contains a contribution from the rare-earth magnetic sublattice. In the following, we model the above-mentioned contribution of the induced Ce moment to the field at the muon site by an additional Curie-Weiss contribution. This can be interpreted as a local magnetization of paramagnetic moments of the Ce sublattice induced by the molecular field generated by the Fe sublattice. In turn, the induced Ce sublattice magnetization creates a dipole field at the muon site. The temperature dependence of the Fe molecular field has to be proportional to the Fe sublattice magnetization, i.e., the muon spin precession frequency $f_\mu(T)$ observed in the other *R*FeAsO systems. This is plausible because we have shown that $f_\mu(T)$ above the rare-earth ordering temperature T_N^R is almost independent of the rare-earth ion. Thus we chose the following function to describe our data in a first approximation:

$$f_\mu(T) = f_0\left[1 - \left(\frac{T}{T_N^{\mathrm{Fe}}}\right)^\alpha\right]^\beta\left[1 + \frac{\tilde{C}}{T-\theta}\right]. \quad (3)$$

The first term in the last square brackets is used to describe the contribution of the Fe sublattice and the second term is the additional Curie-Weiss contribution of the Ce sublattice to the magnetic field $B(T)=2\pi f_\mu(T)/\gamma_\mu$ at the muon site. Here, $\tilde{C}$ describes the hyperfine coupling constant of the Ce moments with the muon spin. A fit of this function to the μSR frequency $f_\mu(T)$ obtained for CeFeAsO is shown in Fig. 3 and the two contributions are highlighted as described in the legend. This simple model describes the data reasonably well for temperatures between 10 K and up to $T_N^{\mathrm{Fe}}=137$ K, yielding $f_0=25.7(5)$ MHz, $\alpha=2.4(4)$, and $\beta=0.24(1)$. The constants $\tilde{C}=2.5(5)$ K and $\theta=-3(0.5)$ K were obtained by restricting the fit range to the most relevant temperature region between 10 and 50 K. The exponents α and β are close to the results obtained for the other systems without the Curie-Weiss contribution. The enhanced f_0 could be due to a slightly different muon site compared to other *R*FeAsO compounds. The deviation from this behavior below 10 K is attributed to the growth of antiferromagnetic correlations in the vicinity of T_N^{Ce}.

The exceptionally strong coupling of the Ce is already reasonable considering the ground-state properties of the *R* ion in the crystal electric field (CEF). The ground state of the Kramers ion Ce^{3+} is the *J* multiplet $^2F_{5/2}$. The Sm^{3+} Kramers ion has $^6H_{5/2}$ as lowest *J* multiplet with $J=5/2$. The non-Kramers ion Pr^{3+} stays in the $^3H_4$ ground multiplet with $J=4$. The magnetic behavior of the *R* ions can be understood qualitatively from the susceptibility of free *R* ions

$$\chi_0(T) = \frac{g_J^2\mu_B^2 J(J+1)}{3T}. \quad (4)$$

Thus, because of the different *g* factors [$g_J(\mathrm{Ce})=6/7$, $g_J(\mathrm{Sm})=2/7$, and $g_J(\mathrm{Pr})=4/5$], one expects at least 1 order of magnitude less induced Sm magnetic moment compared to Ce (for equal magnitudes of Fe-Sm and Fe-Ce coupling constants, see Sec. V B). Probably, due to this feature, we observe very similar μSR spectra in the Sm, Pr, and La compounds in the temperature range $T_N^R < T < T_N$. Since the exact sequence of CEF levels in PrFeAsO is not known up to now, it is more difficult to predict its behavior.

The above qualitative discussion neglects higher CEF levels and the Ce-Ce interactions. A more detailed and quantitative discussion of the coupling of the Ce sublattice to the Fe sublattice using classical and quantum approaches will be given in Secs. V and VI.

B. Rare-earth magnetic order

For $R=$Pr and Ce, the onset of the rare-earth magnetic order 11(1) and 4.4(3) K, respectively, causes a second order, i.e., smooth decrease of the muon precession frequency $f_\mu(T)$ by approximately ≈ 2.2 MHz at ≈ 2 K in both cases, as can be seen in Fig. 3. However, in PrFeAsO, the Pr magnetic order is accompanied by a maximum in the width ΔB of the magnetic field distribution, i.e., the relaxation rate λ_T (see inset of Fig. 4) that rapidly decreases at lower temperatures, whereas in CeFeAsO, the Ce magnetic order causes the field distribution to broaden monotonically. Note that the magnetic field at the muon site caused by the static order of the Ce sublattice leads to a decrease of the observed μSR frequency while the Fe order induced magnetization of the Ce sublattice above T_N^{Ce} causes an increase of the frequency $f_\mu(T)$. Therefore, it is evident that the Ce moments order in a different structure than induced by the Fe magnetic system.

SmFeAsO shows first-order Sm magnetic order, i.e., the Sm magnetic order parameter is discontinuous at $T_N^{\mathrm{Sm}}=4.66(5)$ K. Contrary to the Ce and Pr magnetic orders, the Sm magnetic order causes the appearance of two satellite muon precession frequencies $f_\mu^{1,2}(T)=f_\mu^0(T)\pm 8.0(5)$ MHz in addition to the main frequency $f_\mu^0(T)$ observed above T_N^{Sm}. The two satellites and the main frequency have signal fractions of 1.0(3):1.0(3):4.3(6). This shows that the Sm magnetic order has different symmetry compared to the Fe magnetic order, i.e., it causes a change of the magnetic unit cell. A detailed discussion of *R* magnetic structures and its interplay with the Fe sublattice will be given in Secs. VI–VIII.

IV. DETERMINATION OF THE MUON SITE

To determine the contributions from Fe and *R* magnetic orders to the local magnetic field at the muon site, it is necessary to determine the muon site in the lattice. For this purpose, we used a modified Thomas-Fermi approach[30] and available structural data. The goal is to determine a self-consistent distribution of the valence electron density from which the electrostatic potential can be deduced. The local minima of this potential at interstitial positions are regarded as possible stopping sites for muons. We verified the applicability of our approach by comparison of numerical results to experimentally determined muon sites in $R\mathrm{FeO}_3$ (Ref. 31) and by a successful interpretation of μSR spectra of the complex magnetic structures in layered cobaltites $R\mathrm{BaCo}_2\mathrm{O}_{5.5}$.[32]

A potential map of CeFeAsO in the *Cmma* orthorhombic phase was calculated using structural data[16] at 1.4 K and is

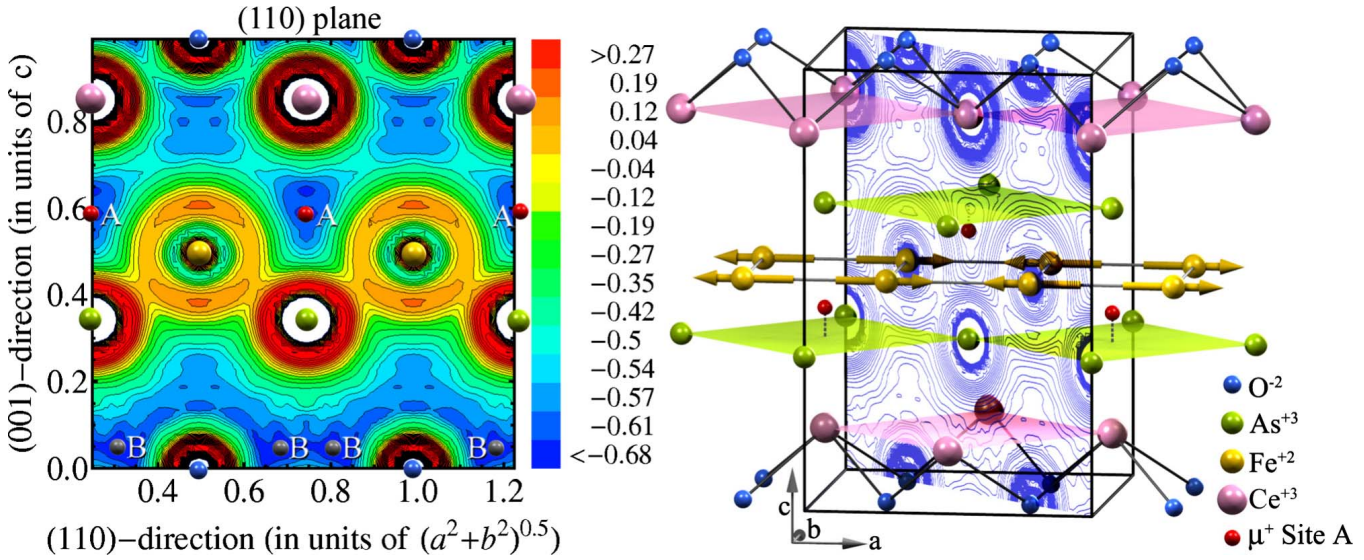

FIG. 5. (Color online) Structure and electrostatic potential-energy map of the (110) plane for a muon in the *Cmma* orthorhombic phase of CeFeAsO. The A and B muon positions are marked by corresponding letters. The potential energy is given in atomic units. The origin of the unit cell has been moved for clarity.

shown in Fig. 5. The calculations have been done without taking into account the host-lattice relaxation around the muon. We observe two types of possible muon positions which are labeled A and B. The *A*-type position is located on the line connecting the Ce and As ions along the *c* direction. Note that a similar location of the point with deepest potential was calculated for LaOeAs in the tetragonal phase using the general potential linearized augmented plane-wave method and local-density approximation.[37] The *A*-type position with coordinates $(0,1/4,z_A)$ has 4*g* local point symmetry *mm*2, i.e., the same as the *R* sites. The B-type position has a general 16*o* local point symmetry with (x,y,z_B) coordinates. For CeFeAsO, the coordinates of A are (0,1/4,0.41) and (0.44,0.19,0.04) for B. Note that the points B are located at oxygen ions which are typical points for muons in many oxides. The z_A and z_B coordinates vary in the third decimal if Ce is replaced by La, Pr, or Sm.

A second important result is the comparison of the calculated muon precession frequency, i.e., the local magnetic-dipole field at the muon site with the experimentally determined muon precession frequency $f_0=f_\mu(T\rightarrow 0)$ for LaFeAsO. With the experimentally determined Fe magnetic moment[13] of $0.36\mu_B$, we calculate $f_{0,\mathrm{A}}=12.4$ MHz for site A and $f_{0,\mathrm{B}}=1.3$ MHz for site B. As shown by Klauss *et al.* in Ref. 12 and Sec. III of this work, in LaFeAsO two muon frequencies are observed. One frequency with 23 MHz originating from the mayor volume fraction ($P=0.7$) and one lower frequency with 3 MHz which develops from a strongly damped signal below approximately 70 K. In *R*FeAsO, with *R*=Sm, Pr, and Ce, only the high frequency is present in the μSR spectra. We conclude that site A is the main muon site since this gives the correct order of magnitude for f_0. Probably, the site B is also partially populated at low temperatures in the LaFeAsO. The fact that we obtain a 46% smaller value than the experimental result is reasonable since our calculation only takes into account local dipole fields and neglects contact hyperfine contributions. Similar differences are found in La_2CuO_4, the antiferromagnetic parent compound of the 214 cuprate superconductors.[53] As will be shown below, the magnetic field caused by the Fe magnetic order is directed along the crystallographic *c* axis. This is in agreement with recent μSR experiments on Fe pnictide single crystals.[44] In the following, we use only muon site A and a renormalization factor of 1.86 for the local field caused by Fe magnetic ordering at this muon site to account for the contact hyperfine field for all *R*. This assumption is justified from our calculation of the electronic charge-density distribution that shows very similar results for all *R*. This manifests itself in the almost identical position of muon site A in compounds with different *R*. In its turn, this means that the renormalization due to the contact hyperfine interaction, which depends only on the electron density at the muon site, should be nearly the same within this series.

V. SYMMETRY ANALYSIS OF FE AND *R* MAGNETIC ORDER PARAMETERS IN *R*FeAsO

A. Translational symmetry and magnetic modes in *R*FeAsO compounds

Iron magnetic order in *R*FeAsO sets in about 10–20 K below the tetragonal to orthorhombic structural phase transition.[13] The space group of the paramagnetic phase is *Cmma* with Fe and *R* ions occupying 4*b* and 4*g* positions, respectively. Neutron studies of *R*FeAsO compounds revealed numerous magnetic Bragg peaks all of which can be reduced just to three types of magnetic propagation vectors.[11,13,16,17,22,43,47] These vectors in an orthorhombic setting are

$$\mathbf{K}_{\mathrm{I}}=(1,0,1/2),$$

$$\mathbf{K}_{\mathrm{II}}=(1,0,0),$$

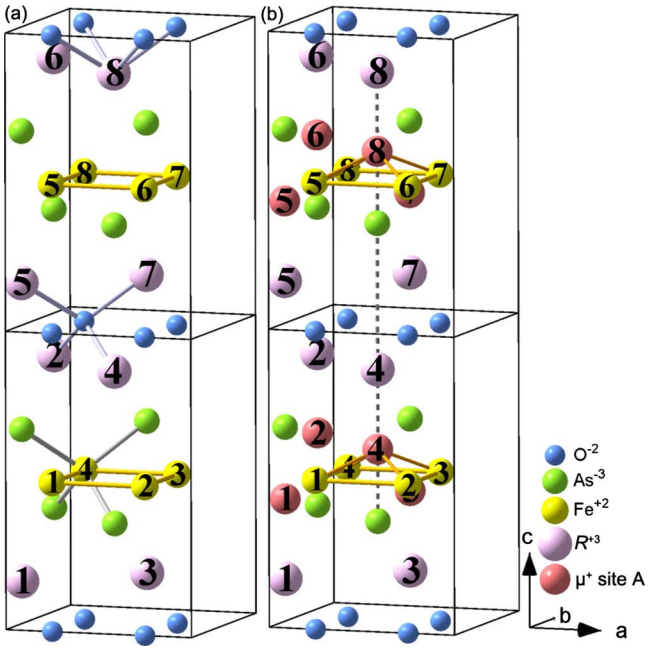

FIG. 6. (Color online) Enumeration of positions used to describe different types of Fe and *R* magnetic orders. (a) *R* and Fe positions and (b) muon site A.

$$\mathbf{K}_{\mathrm{III}} = (0,0,1/2). \tag{5}$$

Here we use an orthorhombic primitive cell with the unit-cell vectors $\mathbf{a}_O = 2\tau_x \mathbf{e}_a$, $\mathbf{b}_O = 2\tau_y \mathbf{e}_b$, and $\mathbf{c}_O = 2\tau_z \mathbf{e}_c$, where τ_x, τ_y, and $2\tau_z$ are the distances between nearest-neighbor Fe ions along *a*, *b*, and *c* directions, denoted by the unit vectors $\mathbf{e}_i$, respectively. Note that in this setting, nuclear Bragg peaks of the *Cmma* space group are either $(2H,2K,L)$ or $(2H+1,2K+1,L)$. Also, a "magnetic setting" with $\mathbf{a}_m = \mathbf{a}_O$, $\mathbf{b}_m = \mathbf{b}_O$, and $\mathbf{c}_m = 2\mathbf{c}_O$ is often used.

The primitive cells of the magnetic structures induced by each of the $\mathbf{K}_\gamma$ are not orthorhombic. Each of the magnetic primitive cells contains four magnetically inequivalent *R*, Fe, and muon sites. To analyze the symmetry of the magnetic structures in a unified way, we will label these four positions with numbers $\alpha = 1,2,3,4$, with corresponding ordered magnetic moments $\mathbf{m}_\alpha$ for the *R* and Fe positions. To identify the different positions α in the magnetic cell with positions $\beta = 1,2,\ldots,8$ in the nuclear cell (doubled along the *c* direction), we use the mapping $\{\beta_1,\beta_2\} \mapsto \alpha$, where α is one of the four possible positions in the magnetic primitive cell and β_i a position in the nuclear cell as shown in Fig. 6.

The $\mathbf{K}_{\mathrm{I}}$ propagation vector induces a magnetic lattice of $I_c mmm$ type in which the primitive cell is built on the translations $\mathbf{a}_1 = \mathbf{a}_O$, $\mathbf{a}_2 = \mathbf{b}_O$, and $\mathbf{a}_3 = 1/2(\mathbf{a}_O + \mathbf{b}_O) + \mathbf{c}_O$ and the antitranslation along the *z* axis $\mathbf{a}' = \mathbf{c}_O$.[33] Thus, in $\mathbf{K}_{\mathrm{I}}$-type magnetic structures, the following positions are equivalent and mapped as denoted by "↦:" $\{1,7\} \mapsto 1$, $\{2,8\} \mapsto 2$, $\{3,5\} \mapsto 3$, and $\{4,6\} \mapsto 4$.

The primitive cell of the $P_C mmm$ magnetic lattice induced by the $\mathbf{K}_{\mathrm{II}}$ propagation vector is constructed from the translations $\mathbf{a}_1 = \mathbf{a}_O$, $\mathbf{a}_2 = \mathbf{b}_O$, and $\mathbf{a}_3 = \mathbf{c}_O$ and the antitranslation $\mathbf{a}' = 1/2(\mathbf{a}_O + \mathbf{b}_O)$.[33] Then we obtain the identity of the positions $\{1,5\} \mapsto 1$, $\{2,6\} \mapsto 2$, $\{3,7\} \mapsto 3$, and $\{4,8\} \mapsto 4$.

Finally, for the $\mathbf{K}_{\mathrm{III}}$ propagation vector, the magnetic lattice is $C_c mmm$ and the magnetic primitive cell can be built from the translations $\mathbf{a}_1 = 1/2(\mathbf{a}_O + \mathbf{b}_O)$, $\mathbf{a}_2 = 1/2(\mathbf{a}_O - \mathbf{b}_O)$, and $\mathbf{a}_3 = 2\mathbf{c}_O$.[33] Therefore, we have the mappings $\{1,3\} \mapsto 1$, $\{2,4\} \mapsto 2$, $\{5,7\} \mapsto 3$, and $\{6,8\} \mapsto 4$.

In order to investigate the magnetic interactions in different *R* and Fe magnetic structures with the translational symmetry of the propagation vector $\mathbf{K}_\gamma$ ($\gamma \in \{0,\mathrm{I},\mathrm{II},\mathrm{III}\}$), it is necessary to calculate the magnetic modes, i.e., basis functions of the irreducible representations (IRs) of the propagation vector little groups G_γ. These groups are the same for all propagation vectors (5) and they are also identical with the groups for ferromagnetic order, i.e., propagation vector $\mathbf{K}_0 = (0,0,0)$.[34] Following a method described by Bertout[35] and Izyumov and Naish,[36] we introduce possible magnetic modes $\mathbf{F}$ and $\mathbf{L}_i$, $i = 1,2,3$ as linear combinations of Fe (or *R*) sublattice magnetic moments $\mathbf{m}_\alpha$, where α denotes a particular atom (see above) in the respective magnetic primitive cell

$$\mathbf{F} = 1/4(\mathbf{m}_1 + \mathbf{m}_2 + \mathbf{m}_3 + \mathbf{m}_4),$$

TABLE II. Magnetic modes of the magnetic propagation vectors $\mathbf{K}_\gamma$, i.e., basis functions of the irreducible representations τ_ν (see text). The indexes indicate the nonzero Cartesian components of the vectors (6), i.e., for example, L_{1z} is the *z* component of $\mathbf{L}_1$.

Cmma symmetry elements[a]									$\mathbf{K}_0$ (0,0,0)		$\mathbf{K}_{\mathrm{I}}$ $(\pi/\tau_x,0,\pi/2\tau_z)$		$\mathbf{K}_{\mathrm{II}}$ $(\pi/\tau_x,0,0)$		$\mathbf{K}_{\mathrm{III}}$ $(0,0,\pi/2\tau_z)$	
IR	1	2_x	2_{1y}	2_{1z}	$\bar{1}$	m_x	m_{1y}	m_{1z}	Fe	*R* and μ^+	Fe	*R* and μ^+	Fe	*R* and μ^+	Fe	*R* and μ^+
τ_1	1	1	1	1	1	1	1	1	–	–	L_{3y}	–	L_{1x}	–	L_{3z}	–
τ_2	1	1	1	1	−1	−1	−1	−1	–	L^R_{2z}	L_{1y}	L^R_{1z}	L_{3x}	L^R_{3z}	L_{1z}	L^R_{1z}
τ_3	1	1	−1	−1	1	1	−1	−1	F_x	F^R_x	L_{3z}	L^R_{3x}	–	L^R_{1x}	L_{3y}	L^R_{3x}
τ_4	1	1	−1	−1	−1	−1	1	1	L_{2x}	L^R_{2y}	L_{1z}	L^R_{1y}	–	L^R_{3y}	L_{1y}	L^R_{1y}
τ_5	1	−1	1	−1	1	−1	1	−1	F_y	F^R_y	–	L^R_{3y}	L_{1z}	L^R_{1y}	L_{3x}	L^R_{3y}
τ_6	1	−1	1	−1	−1	1	−1	1	L_{2y}	L^R_{2x}	–	L^R_{1x}	L_{3z}	L^R_{3x}	L_{1x}	L^R_{1x}
τ_7	1	−1	−1	1	1	−1	−1	1	F_z	F^R_z	L_{3x}	L^R_{3z}	L_{1y}	L^R_{1z}	–	L^R_{3z}
τ_8	1	−1	−1	1	−1	1	1	−1	L_{2z}	–	L_{1x}	–	L_{3y}	–	–	–

[a]Index 1 denotes an improper translation along the *y* axis.

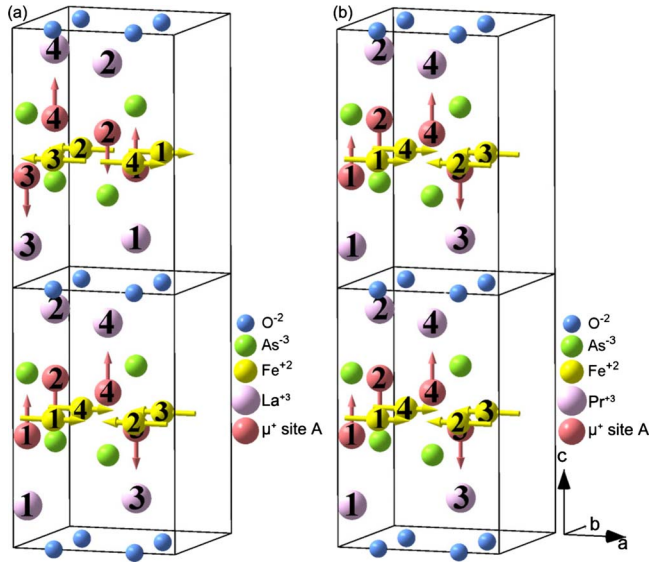

FIG. 7. (Color online) (a) $L_{3x}(\mathrm{K_I})$-type Fe magnetic order realized in LaFeAsO and probably in SmFeAsO and its magnetic-dipole field direction at the muon site A. (b) $L_{3x}(\mathrm{K_{II}})$ order observed in CeFeAsO and PrFeAsO.

$$\mathbf{L}_1 = 1/4(\mathbf{m}_1 + \mathbf{m}_2 - \mathbf{m}_3 - \mathbf{m}_4),$$

$$\mathbf{L}_2 = 1/4(\mathbf{m}_1 - \mathbf{m}_2 + \mathbf{m}_3 - \mathbf{m}_4),$$

$$\mathbf{L}_3 = 1/4(\mathbf{m}_1 - \mathbf{m}_2 - \mathbf{m}_3 + \mathbf{m}_4). \quad (6)$$

The components of these linear combinations are the basis functions of the eight one-dimensional IRs τ_ν with $1 \leq \nu \leq 8$ for the G_0 group (see Table 32 in Ref. 34). The results of the symmetry analysis for the magnetic moments located at the 4*b* positions (Fe ions) and 4*g* positions (*R* ions and muon sites) are shown in Table II.

In accordance with neutron data, the iron magnetic subsystem orders antiferromagnetically along the *a* direction and ferromagnetically along the *b* direction with doubling of the unit cell along the *c* axis for the *R*=La compound (magnetic propagation vector $\mathbf{K_I}$) and without doubling for *R*=Ce and Pr (magnetic propagation vector $\mathbf{K_{II}}$).[43] In all these structures, Fe magnetic moments are directed along the *a* axis. These magnetic structures are described by $L_{3x}(\mathbf{K_I})$ and $L_{3x}(\mathbf{K_{II}})$ nonzero magnetic order parameters shown in Table II.

The onset of a given type of magnetic order lowers the symmetry of the paramagnetic phase and creates a magnetic symmetry. The orientation of the magnetic moments and the distribution of local magnetic fields in the magnetic cell have the same symmetry. To determine the orientation of the magnetic field at a particular muon site, we assign an artificial magnetic degree of freedom to this site. The set of magnetic degrees of freedom for different points (Wyckoff positions) forms a magnetic representation. A standard decomposition of this magnetic representation into irreducible representations of the space group allows the analysis of the symmetry of magnetic field distributions at the muon sites. This symmetry must be compatible with the given space group and the same as the symmetry of the magnetic order parameter. In other words, the symmetry of the magnetic field distribution at the muon site must belong to the same IR as the magnetic order parameter.

From Table II, it becomes self-evident that the $L_{3x}(\mathbf{K_{II}})$ type of magnetic structure of iron moments creates $L^R_{3z}(\mathbf{K_{II}})$-type molecular fields at the rare-earth and *A*-type muon sites. Therefore, a magnetic field distribution of any symmetry that induces a staggered-type ordering of the *R* magnetic moments leads to a magnetic field distribution at the *A*-type muon site of same symmetry. Due to symmetry reasons, some types of Fe magnetic order, for instance $L_{3y}(\mathbf{K_I})$, do not create magnetic fields at the 4*g* positions. Thus, the presence of μSR signals in the Fe antiferromagnetically (AFM) ordered phase of *R*=La, Pr, Ce, and Sm compounds excludes the possibility for AFM magnetic order along the *a* axis and ferromagnetic (FM) order along *b* axis with iron magnetic moments directed along *b* axis.

The $L_{3x}(\mathbf{K_I})$ type of Fe order and the corresponding direction of the magnetic field at the *A*-type muon site are shown in Fig. 7. The dipole fields at the *A*-type muon position for all types of Fe and *R* magnetic order are given in the Appendix.

B. Symmetry of the Fe-*R* magnetic interactions

To start with the strongest exchange interaction, we analyze the symmetry of permutation modes (5) or exchange

TABLE III. Permutation modes, i.e., exchange multiplets of the four magnetic propagation vectors.

	$\mathbf{K}_0$ (0,0,0)		$\mathbf{K}_\mathrm{I}$ $(\pi/\tau_x, 0, \pi/2\tau_z)$		$\mathbf{K}_\mathrm{II}$ $(\pi/\tau_x, 0, 0)$		$\mathbf{K}_\mathrm{III}$ $(0, 0, \pi/2\tau_z)$	
IR	Fe	*R*	Fe	*R*	Fe	*R*	Fe	*R*
τ_1	$\mathbf{F}$	$\mathbf{F}^R$	–	$\mathbf{L}^R_1$	–	$\mathbf{L}^R_1$	–	$\mathbf{L}^R_3$
τ_2	$\mathbf{L}_2$	–	–	–	–	–	–	–
τ_3	–	–	–	–	$\mathbf{L}_1$	–	–	–
τ_4	–	–	–	–	$\mathbf{L}_3$	–	–	–
τ_5	–	–	$\mathbf{L}_3$	–	–	–	$\mathbf{L}_3$	–
τ_6	–	–	$\mathbf{L}_1$	–	–	–	–	–
τ_7	–	–	–	–	–	–	–	–
τ_8	–	$\mathbf{L}^R_2$	–	$\mathbf{L}^R_3$	–	$\mathbf{L}^R_3$	$\mathbf{L}_1$	$\mathbf{L}^R_1$

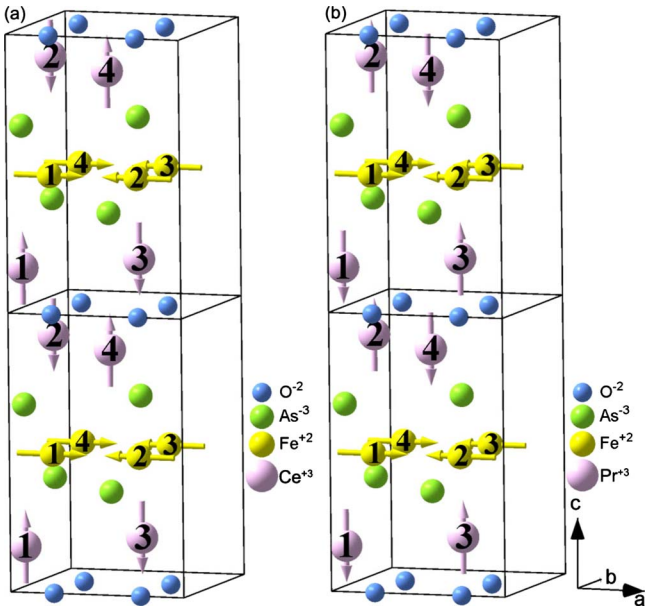

FIG. 8. (Color online) Direction of the magnetic moment on the R site induced by the $L_{3x}(\mathrm{K_{II}})$ Fe order in (a) CeFeAsO and (b) PrFeAsO. The sign of the coupling constant $I_{3xz}^{\text{Fe-}R}$ is different in the Ce and the Pr compounds resulting in opposite orientation of the induced moments.

multiplets for Fe and R magnetic subsystems.[35] The permutation modes for the different translational symmetries $\mathbf{K}_\gamma$ are listed together with the corresponding irreducible representations in Table III.

Since there are no permutation modes of the Fe and R subsystems which belong to the same irreducible representation, there are no Heisenberg exchange interactions between the R and Fe subsystems for the case of $\mathbf{K}_\mathrm{I}$ or $\mathbf{K}_\mathrm{II}$ translational symmetry of the Fe magnetic order. This interaction exists only for magnetic structures with $\mathbf{K}_0$ and $\mathbf{K}_\mathrm{III}$ translational symmetries. The respective Fe-R magnetic exchange Hamiltonian has the form

$$\mathcal{H}_{ex}^{\text{Fe-}R} = \cdots + J_0^{\text{Fe-}R}(\mathbf{K}_0)(\mathbf{F}\cdot\mathbf{F}^R) + J_1^{\text{Fe-}R}(\mathbf{K}_\mathrm{III}) \times(\mathbf{L}_1(\mathbf{K}_\mathrm{III})\mathbf{L}_1^R(\mathbf{K}_\mathrm{III})). \quad (7)$$

However, for the cases of $\mathbf{K}_\mathrm{I}$ and $\mathbf{K}_\mathrm{II}$ translational symmetries, the Fe and R subsystems can interact by the non-Heisenberg exchange (see Table III). The part of these anisotropic Fe-R interactions relevant for the following considerations is given by

$$\begin{aligned}\mathcal{H}_{an\text{-}ex}^{\text{Fe-}R} = \cdots &+ I_{3xz}^{\text{Fe-}R}(\mathbf{K}_\mathrm{I})L_{3x}(\mathbf{K}_\mathrm{I})L_{3z}^R(\mathbf{K}_\mathrm{I}) \\ &+ I_{3zx}^{\text{Fe-}R}(\mathbf{K}_\mathrm{I})L_{3z}(\mathbf{K}_\mathrm{I})L_{3x}^R(\mathbf{K}_\mathrm{I}) \\ &+ I_{3xz}^{\text{Fe-}R}(\mathbf{K}_\mathrm{II})L_{3x}(\mathbf{K}_\mathrm{II})L_{3z}^R(\mathbf{K}_\mathrm{II}) \\ &+ I_{3zx}^{\text{Fe-}R}(\mathbf{K}_\mathrm{II})L_{3z}(\mathbf{K}_\mathrm{II})L_{3x}^R(\mathbf{K}_\mathrm{II}) + \cdots . \end{aligned} \quad (8)$$

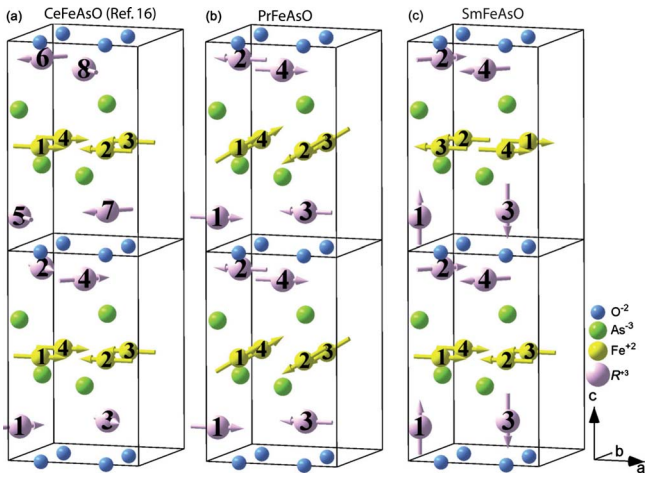

FIG. 9. (Color online) (a) Collinear Fe magnetic order ($\mathbf{K}_\mathrm{II}$) and noncollinear Ce order in CeFeAsO as proposed by Zhao *et al.* (Ref. 16) which is in accordance with the μSR measurements. (b) Magnetic structure of the Pr and Fe subsystems with $\mathbf{K}_\mathrm{II}$ translation symmetry which satisfactorily describes μSR and Mössbauer data. Nonzero are the $L_{3x}\cos\theta + L_{3z}\sin\theta$ of Fe and L_{3x}^R of Pr order parameters. The Fe and Pr subsystems remain in the L_3 and L_3^R types of exchange magnetic order, respectively. (c) The proposed Sm structure which explains the observed μSR spectra. Fe magnetic ordering has $\mathbf{K}_\mathrm{I}$ translational symmetry with a doubling along the c axis, while the Sm magnetic order possesses $\mathbf{K}_\mathrm{II}$ translational symmetry without a doubling along the c axis).

Consequently, the onset of the $L_{3x}(\mathbf{K}_\mathrm{I/II})$ type of Fe magnetic order creates an effective staggered magnetic field at the R site along the z direction. The magnitude of this field is proportional to the value of the Fe-R coupling constant $I_{3xz}^{\text{Fe-}R}$ and the iron subsystem order parameter L_{3x} determines its temperature dependence. In the following, we will show that this field exceeds a respective dipole field at the R sites by at least 1 order of magnitude. The mutual orientation of the L_{3x} and L_{3z}^R vectors depends on the sign of the Fe-R coupling constant $I_{3xz}^{\text{Fe-}R}$. The orientation of the induced magnetic moment on the R site is shown in Fig. 8. The magnitude of the z component of the rare-earth magnetic moments $m_{\alpha z}^R(\alpha = 1-4)$ is determined by the exchange field and the R ion CEF.

VI. DETERMINATION OF THE MAGNETIC STRUCTURES AND THE FE–R COUPLING CONSTANTS FROM THE TEMPERATURE DEPENDENCE OF THE μSR RESPONSE

Below the Néel temperature, the μSR response of RFeAsO is mainly determined by magnetic-dipole fields created by the Fe and R subsystems on the A-type muon site. It can be calculated by

$$B_z(A) = 2.58L_{3x}(\mathbf{K}_\mathrm{I}) + 1.45L_{3z}^R(\mathbf{K}_\mathrm{I}),$$

$$B_z(A) = 2.57L_{3x}(\mathbf{K}_\mathrm{II}) + 1.48L_{3z}^R(\mathbf{K}_\mathrm{II}). \quad (9)$$

If the $L_{ij}(\mathbf{K}_\gamma)$ are given in units of μ_B [see Eq. (6)], the magnetic-dipole field $B_z(A)$ is obtained in units of 0.1 T.

These equations demonstrate a surprisingly close agreement of dipole fields for Fe magnetic order with ($\mathbf{K}_{\mathrm{I}}$) and without ($\mathbf{K}_{\mathrm{II}}$) doubling along z axis. Note that the constants in Eqs. (9) only vary in the third decimal if Ce is replaced by La, Pr, or Sm. This explains the similar μSR spectra of LaFeAsO with $L_{3x}(\mathbf{K}_{\mathrm{I}})$ and CeFeAsO and PrFeAsO both with $L_{3x}(\mathbf{K}_{\mathrm{II}})$ type of Fe antiferromagnetic order. The high-temperature fit of the μSR frequency gives roughly the same saturation value $f_0=\gamma_\mu/2\pi B=23.0(5)$ MHz. This corresponds to a value of $0.36\mu_B$ for the Fe saturation moment if one takes into account contact hyperfine fields by applying the renormalization factor of 1.86 as in LaFeAsO. Because of the similar order parameters of the Fe magnetic order found in SmFeAsO, LaFeAsO, and PrFeAsO, we conclude that a L_{3x} type of Fe antiferromagnetic order is also realized in SmFeAsO. However, μSR studies alone cannot distinguish between the possible translational symmetries, i.e., $\mathbf{K}_{\mathrm{I}}$ and $\mathbf{K}_{\mathrm{II}}$ of the order parameter.

A. CeFeAsO

The μSR response drastically changes below the Ce ordering temperature T_N^{Ce}. Contrary to the naive expectation that the Ce magnetic order would increase the local magnetic field at the muon site and therefore the μSR frequency, our experimental results show a decrease of the μSR frequency below T_N^{Ce}. According to our analysis of the magnetic field distribution at the A-type muon site this behavior indicates a breaking of the L_{3z}^R symmetry of the induced Ce order. Neutron diffraction studies of CeFeAsO revealed the appearance of $\mathbf{K}_{\mathrm{III}}$-type magnetic Bragg peaks below T_N^{Ce} in addition to $\mathbf{K}_{\mathrm{II}}$-type peaks also present above T_N^{Ce}.[16] The Ce magnetic structure proposed by Zhao *et al.* is a noncollinear arrangement of Ce moments in the *ab* plane.[16] This structure is shown in Fig. 9(a) and can be described as a linear combination of two order parameters: $L_{1x}^R(\mathbf{K}_{\mathrm{III}})+L_{3y}^R(\mathbf{K}_{\mathrm{II}})$. This type of R order produces the following magnetic field at the A-type muon site for temperatures below T_N^{Ce}:

$$B_x(A) = -0.40L_{1x}^{\mathrm{Ce}}(\mathbf{K}_{\mathrm{III}}),$$

$$B_y(A) = -0.88L_{3y}^{\mathrm{Ce}}(\mathbf{K}_{\mathrm{II}}),$$

$$B_z(A) = 2.57\frac{f_0}{13.55} + 1.48L_{3z}^{\mathrm{Ce}}(\mathbf{K}_{\mathrm{II}}). \qquad (10)$$

Here, $f_0=25.7$ MHz accounts for the contribution of the iron subsystem, which, we suppose, preserves its magnetic structure found above T_N^{Ce}. Despite different translational symmetry of the Ce order parameters, the magnetic fields at all eight muon sites have the same modulus (10), therefore no additional frequencies appear at temperatures below T_N^{Ce}. With the Ce magnetic moment of $0.83\mu_B$ at 1.7 K reported by Zhao *et al.*[16] and supposing $L_{3z}^{\mathrm{Ce}}=0$, we then obtain a μSR frequency of $f=26.9$ MHz instead of the experimentally observed 29.8 MHz at 1.9 K. Also, the experiment reveals a remarkable decrease of the observed μSR frequency compared to maximal value of 32 MHz at 4 K. The decrease of the μSR frequency is not as rapid as expected; it develops only gradually below T_N^{Ce}. As follows from Eq. (10), the magnetic-dipole fields at the muon sites created by the Ce magnetic moments lie in the *ab* plane and are rather weak compared to the dipole field created by the Fe moments. The slow decrease of the μSR frequency below T_N^{Ce} therefore reflects the gradual disappearance of the Fe-induced L_{3z}^{Ce}-type magnetization of the Ce moments in the AFM Ce phase below T_N^{Ce}. One can conclude that the Ce-Ce coupling constant which creates the $L_{1x}^{\mathrm{Ce}}(\mathbf{K}_{\mathrm{III}})+L_{3y}^{\mathrm{Ce}}(\mathbf{K}_{\mathrm{II}})$ AFM Ce order parameter cannot immediately suppress the induced L_{3z}^{Ce} magnetization. As will be shown below, the Ce-Ce coupling constant $J_{3z}^{\mathrm{Ce}}(\mathbf{K}_{\mathrm{II}})$ is of the same order as the Fe-Ce coupling constant $I_{3xz}^{\mathrm{Fe\text{-}Ce}}(\mathbf{K}_{\mathrm{II}})$. Using Eq. (10), we estimate the remanent order parameter $L_{3z}^{\mathrm{Ce}}=0.14\mu_B$ at 1.9 K.

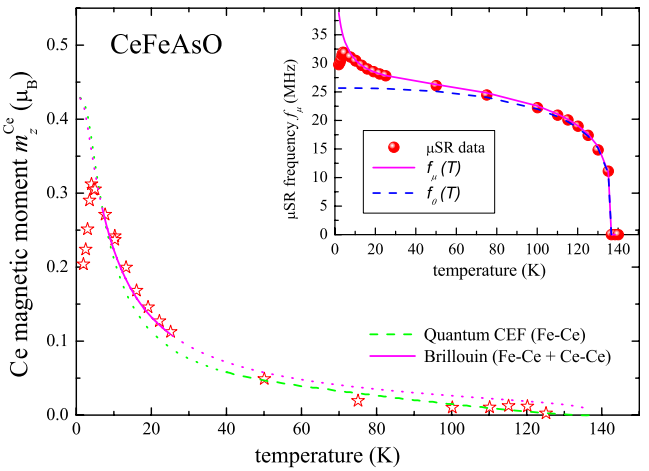

FIG. 10. (Color online) Temperature dependence of the induced Ce magnetic moment $m_z^{\mathrm{Ce}}(T)$ for $T>T_N^{\mathrm{Ce}}$. $m_z^{\mathrm{Ce}}(T)$ has been extracted from the μSR frequency by subtracting the contribution from the Fe subsystem (inset). Data are fitted by a quantum and a Brillouin approach valid in different temperature regions (see text).

Due to the significant contribution of Ce dipole fields, the μSR frequency $f_\mu(T)$ is unusually high already far above T_N^{Ce} in CeFeAsO. This has been discussed phenomenologically in Sec. III. Here we carry out a more elaborate analysis of this observation. The lowest crystal electric field (CEF) states of CeFeAsO and SmFeAsO consist of three Kramers doublets. With the onset of antiferromagnetic iron order, these doublets split. Inelastic neutron-scattering studies of CeFeAsO revealed that in the paramagnetic phase, the energies of the first and the second excited doublets are 216 and 785 K, respectively.[38] The splitting at $T=7$ K amounts to 10.8 K for the ground-state doublet and 37.1 and 66.1 K for the first-excited levels. Using these experimentally deduced parameters and the wave functions of the corresponding CEF levels allows us to determine the Fe-Ce and Ce-Ce exchange interaction coupling constants. In the Fe antiferromagnetic phase above T_N^{Ce}, they are obtained by fitting the theoretical temperature dependence of the Ce magnetic moment $m_z^{\mathrm{Ce}}(T)$ to the experimental data. In Fig. 10, the experimental value of the Ce single-ion magnetic moment $m_z^{\mathrm{Ce}}(T)$ is shown. It is calculated from the μSR frequency f_{exp} with the help of Eq. (9) after subtracting the Fe contribution $f_0(T)$ (see inset of Fig. 10)

$$L_{3z}^{\mathrm{Ce}}(T) = m_z^{\mathrm{Ce}}(T) = [f_{exp}(T) - f_0(T)]/13.55 \cdot 1.48. \quad (11)$$

In this effective-field approximation, the Fe-Ce coupling constant $I_{3xz}^{\mathrm{Fe\text{-}Ce}}(K_{\mathrm{II}})$ and the Ce-Ce coupling constant $J_{3z}^{\mathrm{Ce}}(K_{\mathrm{II}})$ both create a staggered effective field $B_z^{eff}(T)$ on the Ce sites. Its interaction with the Ce magnetic moments lifts the degeneracy of the Kramers doublets. The corresponding effective field on the Ce site is given by

$$B_z^{eff}(T) = B_z^{\mathrm{Fe\text{-}Ce}}(T) + J_{3z} m_z^{\mathrm{Ce}}(T), \quad (12)$$

where $B_z^{\mathrm{Fe\text{-}Ce}}(T) = I_{3xz}^{\mathrm{Fe\text{-}Ce}}(K_{\mathrm{II}}) L_{3x}(T)$ and $J_{3z} = 2J_{3z}^{\mathrm{Ce}}(K_{\mathrm{II}})$ with I and J in units of T/μ_B. We neglect contributions from Fe-Ce and Ce-Ce dipole fields to the splitting of Kramers doublets under the assumption that the Fe-Ce and Ce-Ce (non-)Heisenberg exchange fields [see Eq. (12)] are much stronger. The Fe-Ce staggered field $B_z^{\mathrm{Fe\text{-}Ce}}$ has to have the same temperature dependence as $f_0(T)$, i.e., the averaged value of the iron order parameter $L_{3x}(T)$. Therefore, it can be modeled as $B_z^{\mathrm{Fe\text{-}Ce}}(T) = B_0[1-(T/T_c)^{\alpha}]^{\beta}$, with $\alpha = 2.4$ and $\beta = 0.24$ as determined in Sec. III.

According to the analysis of inelastic neutron-scattering data,[38] the lowest Kramers doublet possesses the orbital momentum $J_z = \pm 1/2$ and does not contain any admixtures of the $J_z = \pm 3/2, \pm 5/2$ states. One can estimate the magnitude of the effective field from the splitting of the ground Kramers doublet at $T = 7$ K by using the relation

$$g_J \mu_B B_z^{eff}(T) = k_B \Delta, \quad (13)$$

where $g_J = 6/7$ is the g factor of the free Ce^{3+} ion and $\Delta = 10.8$ K the splitting of the ground-state doublet. If we account for just the Fe-Ce interaction, it yields $B_0 = 18.75$ T. This large Fe-Ce effective field indicates that dipole-dipole interactions (see the Appendix, Sec. 2) do not play a significant role for the magnetization of the Ce sublattice by the ordered Fe sublattice above T_N^{Ce}.

The temperature dependence of the Ce moment in the effective field has been calculated in a quantum-mechanical approach according to Eq. (10) in Ref. 42 by calculating the thermal population of all experimentally determined CEF levels.[38] The result is shown in Fig. 10 as a dashed green line. From our calculation, it is clear that there is a deviation from Curie-Weiss behavior due to a sizable contribution to m_z^{Ce} from higher Kramers doublets for temperatures above 50 K. In Sec. III, we did a Curie-Weiss approximation of m_z^{Ce} by using Eq. (3). A Curie-Weiss description neglects higher crystal-field levels. This is the reason why we restricted the fit to the temperature range between 10 and 50 K in the first approximation done in Sec. III.

On the other hand, a systematic deviation between m_z^{Ce} obtained from the quantum approach and the experimental data is observed in the low-temperature region between 10 and 50 K. This indicates that the Ce-Ce interaction, which is neglected by this approach, is significant in this temperature region and has to be taken into account for a proper description of the data. Therefore, we fit the Ce magnetic moment with contributions from the Fe-Ce and Ce-Ce exchange interactions by using the usual Brillouin function. In the case of $S = 1/2$, this leads to the following equation:

$$m_z^{\mathrm{Ce}}(T) = \frac{g_J \mu_B}{2} \tanh\left(\frac{g_J \mu_B}{2 k_B T} B_z^{eff}(T)\right), \quad (14)$$

where B_z^{eff} is given in Eq. (12) which should fulfill the boundary condition given by Eq. (13). This approach neglects the higher crystal-field levels and therefore can only be applied at temperatures below 50 K. From a fit in the low-temperature region, we obtain the microscopic parameters $B_0 = 26.8(5)$ T and $J_{3z} = -24.3(5)$ T/μ_B. The fit is shown as a magenta line in the Fig. 10. Using $0.41\mu_B$ for iron-saturated moment, one can estimate a rather large Fe-Ce coupling constant $I_{3xz}^{\mathrm{Fe\text{-}Ce}}(K_{\mathrm{II}}) = 65.3$ T/μ_B. The negative sign of the Ce-Ce coupling constant $J_{3z}^{\mathrm{Ce}}(K_{\mathrm{II}}) = -12.15$ T/μ_B indicates that the L_3^{Ce} type of Ce exchange magnetic order is energy favorable. From $T_N^R = 4.4$ K, one can estimate the value of the $J_{3y}^{\mathrm{Ce}}(K_{\mathrm{II}})$ coupling constant. It is responsible for the appearance of the in-plane L_{3y}^{Ce} order parameter.[16] This rough estimate gives $J_{3y}^{\mathrm{Ce}}(K_{\mathrm{II}}) = -14.9$ T/μ_B. Note that the big difference between Ce-Ce exchange coupling constants along z and y directions points to a strong easy-plane anisotropy in the Ce subsystem.

In conclusion, for CeFeAsO we found a sizable staggered magnetization of the Ce ions induced by the Fe subsystem already far above T_N^{Ce} which amounts to approximately $0.3\mu_B$ near to T_N^{Ce}. With the help of a symmetry analysis as well as classical and quantum-mechanical approaches, we were able to deduce Fe-Ce and Ce-Ce exchange coupling constants. We demonstrated that in the Ce compound, the Fe-Ce non-Heisenberg exchange interaction is exceptionally strong and of the same order as the Ce-Ce exchange interaction. The observed μSR frequency in the Ce ordered phase is in agreement with the magnetic structure proposed by Zhao *et al.*,[16] but a small component from the L_{3z}^{Ce}-type Ce magnetic order induced by the Fe sublattice has to be included to fully explain our data below T_N^{Ce}.

B. PrFeAsO

The ground-state $^3H_4$ multiplet ($J=4$) of the non-Kramers ion Pr^{3+} in the C_{2v} low-symmetry crystal field splits into nine singlets. Since the exact structure of the CEF levels is not known, the Pr^{3+} magnetic susceptibility cannot be estimated. The temperature dependence of the μSR frequency in PrFeAsO is similar to the one observed in LaFeAsO. This suggests that the induced Pr moment is not as strong as in CeFeAsO. However, the comparison of the high-temperature fit of the μSR frequency for La, Ce, Sm, and Pr compounds yields the lowest value of $f_0 = 22$ MHz for the Pr compound. Additionally, there is a small but systematic deviation between μSR and Mössbauer data for PrFeAsO in the Fe AFM phase. This demonstrates that also in PrFeAsO, an Fe-induced ordered Pr moment is present in the Fe AFM phase. One can conclude that, in contrast to the Ce compound, the Fe-Pr coupling constant $I_{3xz}^{\mathrm{Fe\text{-}Pr}}(\mathbf{K}_{\mathrm{II}})$ is small and negative. According to Eq. (9), the fields created by the Fe order parameter L_{3x} and the induced Pr order parameter L_{3z}^{Pr} then have to point in opposite directions at the muon site. Therefore, the μSR frequency in PrFeAsO in the Fe AFM phase is smaller compared to the one in the other compounds.

Recent neutron-diffraction studies reveal that in the Pr-ordered phase the Pr moments are directed along the c axis, which creates a L_{3z}^{Pr} nonzero magnetic order parameter, i.e., the same basis function of the irreducible representation as the induced Pr moments in the Fe ordered phase.[17] Therefore, it is reasonable to assume that also in the Pr-ordered state, the local field at the muon site created by the Fe and the Pr magnetic orders have opposite signs. Respective magnetic structures are shown in Fig. 8(b). The magnetic structure shown can therefore qualitatively explain the 2 MHz drop of the μSR frequency in the Pr-ordered phase. However, the quantitative evaluation of the μSR frequency using Eq. (9) and the Fe and Pr moments of $0.48\mu_B$/Fe and $0.84\mu_B$/Pr at 5 K that were deduced from neutron measurements[17] reveal a strong discrepancy. If the suggested magnetic structure would be realized, a μSR frequency near to zero should have been observed. Even if one includes a strong increase of the local Fe moment (neglecting all transferred hyperfine field contributions) below the Pr ordering temperature which might be suggested by the Mössbauer data,[23] the calculated μSR frequency is much too small. To remove the discrepancy between neutron and μSR observations, one has to conclude that in the PrFeAsO, the Pr magnetic structure is either easy-plane noncollinear or collinear. In this case, the situation would be similar to the Ce and Nd compounds where in addition to the $L_{3z}^{\mathrm{Pr}}(\mathbf{K}_{\mathrm{II}})$ order parameter also other ab plane components such as $L_{3x}^{\mathrm{Pr}}(\mathbf{K}_{\mathrm{II}})$ or $L_{3y}^{\mathrm{Pr}}(\mathbf{K}_{\mathrm{II}})$ exist. Similar conclusions have been drawn from recent neutron-diffraction studies.[11] The consequences of noncollinear order parameters will be discussed in Sec. VII.

C. SmFeAsO

Compared to La and Pr, the Sm compound demonstrates a very similar μSR response in the Fe-ordered AFM phase which implies a $L_{3x}(\mathbf{K}_{\mathrm{I}})$ or $L_{3x}(\mathbf{K}_{\mathrm{II}})$ magnetic Fe order parameter. In spite of the similarity of the lowest CEF levels in Sm and Ce compounds, the low value of the Sm g factor reduces the induced Sm magnetic moment and therefore its contribution to the μSR frequency in the Fe AFM phase. While in the Sm ordered phase, in contrast to the Pr and Ce compounds, the μSR spectra change drastically and several well-resolved frequencies are observed. At the lowest temperatures, three μSR frequencies are observed: 15, 23, and 31 MHz for which the approximate ratio of amplitudes is 1:4:1. This behavior indicates that for the given magnetic symmetry of the Sm order, at least three muon sites are inequivalent. This inequivalence can be caused by different translational symmetry of Sm and Fe magnetic order parameters or a complex noncollinear magnetic order of the Sm subsystem. A minimal model which can explain the μSR spectra involves a $L_{3x}(\mathbf{K}_{\mathrm{I}})$ order parameter for the Fe subsystem with K_{I} and $1/2[L_{1z}^{\mathrm{Sm}}(\mathbf{K}_{\mathrm{II}})+L_{3z}^{\mathrm{Sm}}(\mathbf{K}_{\mathrm{II}})]$ and $1/\sqrt{8}[L_{1x}^{\mathrm{Sm}}(\mathbf{K}_{\mathrm{II}})-L_{3x}^{\mathrm{Sm}}(\mathbf{K}_{\mathrm{II}})+L_{1y}^{\mathrm{Sm}}(\mathbf{K}_{\mathrm{II}})-L_{3y}^{\mathrm{Sm}}(\mathbf{K}_{\mathrm{II}})]$ order parameters for the Sm subsystem with K_{II} translational symmetries. This magnetic structure is shown in Fig. 9(c). It results in three inequivalent muon sites. The first with a low local field at the muon positions (15 MHz at A5 and A7), the second where the field from the R system cancels (23 MHz at A2, A4, A6, and A8), and a third with a high local field (31 MHz at A1 and A3). The experimentally observed amplitudes are also reasonably well reproduced by the model. Within this magnetic model, the size of the Sm magnetic moment can be estimated to be $0.4\mu_B$/Sm at 1.9 K. Note that it is possible to fit the low-temperature data with even more frequencies. The present statistical accuracy is not sufficient to determine the correctness of such a fit, but in a recent μSR study, the low-temperature data have been fitted with five frequencies.[41] One has to note that our symmetry analysis also allows more complicated and even incommensurate Sm magnetic structures.[50]

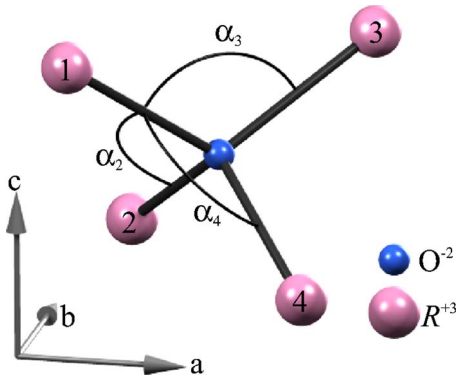

FIG. 11. (Color online) The angle enumeration for R-O-R magnetic bonds in the rare-earth tetrahedron of RFeAsO (R = Pr, Sm, Ce).

VII. RARE-EARTH NONCOLLINEAR ORDER IN RFeAsO

The above-proposed R magnetic structures for the Ce, Sm, and probably also in the Pr compounds involve the well-known exchange noncollinearity, i.e., a perpendicular orientation of neighboring R moments. As shown above, such a magnetic structure can be described by a composition of the Cartesian components of two different permutation modes such as $L_{1x}^{R}(\mathbf{K}_{\mathrm{III}})+L_{3y}^{R}(\mathbf{K}_{\mathrm{II}})$ in the case of the Ce compound or such as $1/2[L_{1z}^{R}(\mathbf{K}_{\mathrm{II}})+L_{3z}^{R}(\mathbf{K}_{\mathrm{II}})]$ in the case of SmFeAsO. From a pure symmetry point of view, commensurate and noncollinear magnetic order is characteristic for crystallographic structures with higher than orthorhombic symmetry that implies existence of two- or three-dimensional IR for their space groups at $k=0$. From a pure energy point of view, the exchange noncollinearity results in competition of two or three different types of exchange multiplets (permutation modes) which belong to the same IR and therefore possess the same Heisenberg energy. In high-symmetry magnets, this competition is resolved by accounting for fourth- or higher-order magnetic interactions in the system's free energy.[45,46] Due to its crystallographic structure, the condition for accidental energy degeneracy of L_1^R and L_3^R rare-earth permutation modes is fulfilled in the RFeAsO compounds. The part of the Hamiltonian containing the R-R exchange interactions for K_{II} translational symmetry can be written in the form

$$\mathcal{H}_{ex}^{R\text{-}R} = \cdots + J_1^R(\mathbf{L}_1^R)^2 + J_3^R(\mathbf{L}_3^R)^2 + \cdots, \qquad (15)$$

where

$$J_1^R = K_{11}^{R\text{-}R} + K_{12}^{R\text{-}R} - K_{13}^{R\text{-}R} - K_{14}^{R\text{-}R} \tag{16}$$

and

$$J_3^R = K_{11}^{R\text{-}R} - K_{12}^{R\text{-}R} - K_{13}^{R\text{-}R} + K_{14}^{R\text{-}R}. \tag{17}$$

For simplicity, we omit the notation K_{II}. The symbol $K_{1\beta}^{R\text{-}R}$ denotes an exchange interaction coupling constant between nearest-neighbor rare-earth ions on sites 1 and β (see Fig. 11). To deduce Eq. (15), we used a permutation symmetry in which the interaction between ions 2 and 4 is equal to the interaction between 1 and 3 and so on. If the exchange constant J_α^R is negative and less than the others J_β^R $(\beta \neq \alpha)$ and a L_α^R type of exchange magnetic order is realized, i.e., the relative orientation of magnetic moments (parallel/antiparallel) in the magnetic structure yields a nonzero L_α^R order parameter as given by Eq. (6).

Neutron diffraction reveals a collinear L_3^R type of rare-earth exchange magnetic order in PrFeAsO (L_{3z}^{Pr} nonzero magnetic order parameter) (Ref. 17) and in NdFeAsO (superposition of L_{3x}^{Nd} and L_{3z}^{Nd} nonzero magnetic order parameters).[47] Similar magnetic structures have been proposed by a theoretical investigation of magnetic order in *R*FeAsO for *R*=Ce, Pr.[48] The authors of Ref. 48 claimed that the *R* magnetic ground state is composed from two adjacent zigzag rare-earth chains running along the *a* axis which carry alternating up and down spins. In our notation, this is the L_3^R type of exchange magnetic order. However, for the Ce compound, this theoretical conclusion is not compatible with experimental data.

A possible reason for the observed noncollinearity is provided by structural features of *R*FeAsO. Note that without orthorhombic distortion, i.e., in the tetragonal $P4/nmm$ phase, two exchange constants $K_{12}^{R\text{-}R}$ and $K_{14}^{R\text{-}R}$ are equal to each other and therefore their contributions to J_1^R and J_3^R cancel. Moreover, even in the orthorhombic *Cmma* phase, their impact should be small. Indeed, the sign of *R*-*R* nearest-neighbor (NN) superexchange depends on the *R*-O-*R* angle. There is a critical value of this angle at which the exchange coupling constant changes its sign. For instance, for Cu-O-Cu bond, this critical angle is equal to 104°.[49] The exchange interaction is antiferromagnetic for magnetic bonds with angles higher than this critical angle. In the Ce compound, the angles of Ce(1)-O-Ce(2) and Ce(1)-O-Ce(4) magnetic bonds, depicted in the Fig. 11 as α_2 and α_4, have values of α_2=105.39° and α_4=105.85° at T=1.4 K while the Ce(1)-O-Ce(3) angle is α_3=117.49°.[16] For NdFeAsO, the respective angles are α_2=105.13°, α_4=105.58°, and α_3=118.06° at T=0.3 K.[47]

The angles α_2 and α_4 are always very similar in *R*FeAsO. This implies that the exchange constants are also similar even if the value is far from the critical angle. The value is far from the critical angle that has been determined for the Cu-O-Cu bond, but might well be near critical for the *R*-O-*R* magnetic bonds considered here. The difference between Ce(1)-Ce(2) and Ce(1)-Ce(4) distances is only 0.011 Å.[16] Therefore, mainly antiferromagnetic exchange $K_{13}^{R\text{-}R} > 0$ determines the magnitude of the J_1^R and J_3^R coupling constants. In the limit of $J_1^R = J_3^R = J^R$, the corresponding exchange Hamiltonian is

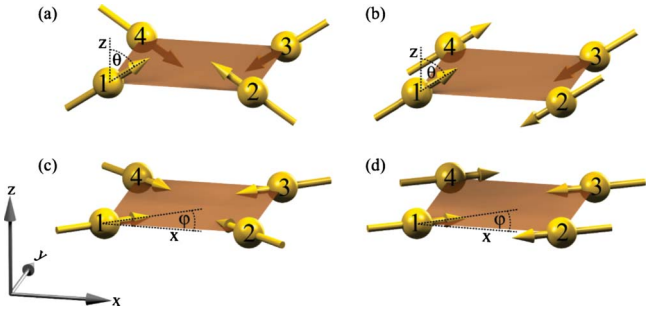

FIG. 12. (Color online) Different types of canted Fe structures that are induced by different rare-earth magnetic structures. (a) Out-of-plane noncollinear Fe order ($L_{3x}\cos\theta + L_{1z}\sin\theta$) induced by L_{1y}^R-type rare-earth order. (b) Out-of-plane collinear Fe order ($L_{3x}\cos\theta + L_{3z}\sin\theta$) induced by L_{3x}^R-type rare-earth order. (c) In plane noncollinear Fe order ($L_{3x}\cos\phi + L_{1y}\sin\phi$) induced by L_{1z}^R-type rare-earth order. (d) In plane collinear Fe order ($L_{3x}\cos\phi + L_{3y}\sin\phi$). Here, θ and ϕ are the polar angles between the Fe(1) magnetic moment and the z axis and the x axis, respectively.

$$\mathcal{H}_{ex}^{R\text{-}R} = J^R[(\mathbf{L}_1^R)^2 + (\mathbf{L}_3^R)^2] = 1/8 J^R[(\mathbf{m}_1^R - \mathbf{m}_3^R)^2 + (\mathbf{m}_2^R - \mathbf{m}_4^R)^2]. \tag{18}$$

Using Eq. (18), one can qualitatively explain the features of *R* magnetic order in the *R*FeAsO compounds. In the *R*-O-*R* layer, both planes of the *R* ions order antiferromagnetically with nonzero antiferromagnetic vectors $\mathbf{l}_1^R = \mathbf{m}_1^R - \mathbf{m}_3^R$ and $\mathbf{l}_2^R = \mathbf{m}_2^R - \mathbf{m}_4^R$ for *R* planes which are located above and below the oxygen plane, respectively. However, these two rare-earth planes are not magnetically coupled, i.e., the mutual orientation of those vectors is not defined by a Heisenberg exchange interaction. This magnetic frustration can be lifted by higher-order interactions such as biquadratic exchange $D^R[(\mathbf{L}_1^R)^2 - (\mathbf{L}_2^R)^2]^2 \propto D^R(\mathbf{l}_1^R \cdot \mathbf{l}_2^R)^2$.[45] For the case of $J^R < 0 < D$, this results in a noncollinear magnetic ground state with $\mathbf{l}_1^R \perp \mathbf{l}_2^R$. Note that this is exactly the spin structure proposed for SmFeAsO in this study and that it is very similar to the one proposed by Zhao *et al.*[16] for CeFeAsO which is also consistent with our data. For the case $J^R < 0$, $D < 0$, a collinear structure with $\mathbf{l}_1^R \| \mathbf{l}_2^R$ is obtained. This structure is realized in NdFeAsO and probably also in PrFeAsO. The actual orientation of the *R* magnetic moments is determined by the complex hierarchy of second-order anisotropy and fourth-order interactions.[50] The orthorhombic distortions observed in the *R*FeAsO system should lead to a weak coupling of antiferromagnetic *R* planes below and above the oxygen plane. Up to now, only the *R*-O-*R* exchange paths have been considered. Note that an inclusion of the *R*-As-*R* exchange paths does not change the proposed scenario because the *R*-As-*R* magnetic bonds only contribute to the $K_{13}^{R\text{-}R}$ exchange and not to the *R*(1)-*R*(2) and *R*(1)-*R*(4) exchanges. The hypothetical case where the ferromagnetic *R*(1)-As-*R*(3) exchange cancels the antiferromagnetic *R*(1)-O-*R*(3) exchange is very unlikely.

VIII. INFLUENCE OF THE *R* MAGNETIC ORDER ON THE FE SUBLATTICE

In the above discussion, we focused on the action of the Fe order on the *R* subsystem. In accordance with Table II and

the Hamiltonian (8), the L_{3x} Fe order parameter creates a molecular field on the R sites which is directed along z axis and has a L^R_{3z} symmetry. The reverse action of the R magnetic order on the Fe subsystem should also be taken into account. This action will be especially important for a realization of the easy-plane anisotropy in the R subsystem when the rare-earth and iron order parameters possess different symmetry. The onset of the L^R_{3x} or L^R_{1y} in plane R order parameters will induce an out-of-plane canting of the iron moments along the z axis due to these Fe-R interactions

$$\begin{aligned}\mathcal{H}^{\text{Fe-}R}_{an\text{-}ex} = \cdots &+ I^{\text{Fe-}R}_{3xz}(\mathbf{K}_{\text{II}})L_{3x}(\mathbf{K}_{\text{II}})L^R_{3z}(\mathbf{K}_{\text{II}}) \\ &+ I^{\text{Fe-}R}_{3zx}(\mathbf{K}_{\text{II}})L_{3z}(\mathbf{K}_{\text{II}})L^R_{3x}(\mathbf{K}_{\text{II}}) \\ &+ I^{\text{Fe-}R}_{1zy}(\mathbf{K}_{\text{II}})L_{1z}(\mathbf{K}_{\text{II}})L^R_{1y}(\mathbf{K}_{\text{II}}) \\ &+ I^{\text{Fe-}R}_{3yz}(\mathbf{K}_{\text{II}})L_{1y}(\mathbf{K}_{\text{II}})L^R_{1z}(\mathbf{K}_{\text{II}}) + \cdots . \qquad (19)\end{aligned}$$

Interestingly, on one hand, the noncollinearity in the R system (L^R_{3z} and L^R_{1y} order parameters) also induces a noncollinearity in the Fe order (L_{3x} and L_{1z} order parameters). On the other hand, a collinear and oblique R magnetic order (L^R_{3x} and L^R_{3z} order parameters) induces a Fe magnetic structure which is still collinear but the Fe moments deviate from the x direction. Different types of canted Fe structures are shown in Fig. 12.

We discuss now whether a canting of the magnetic structures could be observed by μSR and Mössbauer spectroscopy. Here we consider the contribution from the Fe sublattice only. Supposing that the size of the Fe magnetic moment does not change below the R ordering temperature, i.e., it is close to saturation, the μSR response is affected by the canting in the following way. From the dipole field calculation presented in the Appendix, Sec. 1, it follows that the magnetic field at the muon site created by both noncollinear Fig. 12(a) and collinear Fig. 12(b) out-of-plane structures is tilted by the out-of-plane angle θ but does not change its modulus. Therefore, μSR experiments on powder samples cannot distinguish the canted structures from the original collinear L_{3x} structure. In contrast, the field at the muon site, i.e., the μSR frequencies, depends on the angle ϕ for in-plane canted structures shown in Figs. 12(c) and 12(d). In the case of the magnetic structure shown in Fig. 12(d), the μSR frequency always decreases like $\cos\phi$, whereas, in the case of structure (c) in Fig. 12, the field at the muon site may decrease or increase depending on the sign of ϕ and has the following angle dependence: $\sqrt{2}\cos(\phi+\pi/4)$. In turn, its sign determines the sign of the coupling constant $I^{\text{Fe-}R}_{3yz}$ of the Fe-R interaction.

Mössbauer spectroscopy, in contrast to μSR, should be very sensitive to the orientation of the Fe moments. Our calculation of the electric field gradient tensor on Fe site reveals a strong anisotropy with the largest component in the z direction. This makes Mössbauer spectroscopy a suitable tool to detect the direction of the Fe magnetic moment especially in the case where out-of-ab-plane deviations from x axis are present. Again supposing an almost constant modulus of the iron moments below T^R_N, one can derive a strong increase of the quadrupole shift along with an increase of the average hyperfine field for the out-of-plane canted iron structures such as those shown in Figs. 12(a) and 12(b). This behavior has already been detected in the Mössbauer studies of PrFeAsO.[23] McGuire *et al.* came to the conclusion that the Fe spin reorientation with a significant component of Fe moment along the c axis takes place below the Pr-ordering temperature. For the in-plane collinear and noncollinear canted structures shown in Figs. 12(c) and 12(d), the dependence of Mössbauer spectra on the rotation angle ϕ should be weaker than for out-of-plane rotation since it only changes the asymmetry parameter of the electric field gradient tensor.

Combining both comments above, one can understand why the drastic change of PrFeAsO Mössbauer spectra below T^{Pr}_N has no analogy in the μSR spectra. The following model can unify both observations:

(i) In the Pr subsystem, the L^R_3 type of exchange order is realized with an easy-plane anisotropy.

(ii) The order parameter which appears below T^{Pr}_N is L^{Pr}_{3x} with a small induced L^{Pr}_{3z} component remaining even down to the lowest temperatures due to the Fe molecular field $I^{\text{Fe-Pr}}_{3xz}(\mathbf{K}_{\text{II}})L_{3x}(\mathbf{K}_{\text{II}})$. The latter component being negative as mentioned above.

(iii) Below T^{Pr}_N, the in-plane collinear Fe magnetic structure gradually rotates into the collinear out-of-plane $L_{3x}\cos\theta+L_{3z}\sin\theta$ structure.

Respective magnetic fields at the muon sites expressed in MHz are given by

$$B_x(A) = f_0 \sin\theta - 13.55\cdot 0.59 L^{\text{Pr}}_{3x}(\mathbf{K}_{\text{II}}),$$

$$B_z(A) = f_0 \cos\theta. \qquad (20)$$

Here, f_0 is the low-temperature frequency extrapolated from temperatures well above T^{Pr}_N in the Fe antiferromagnetic phase. It is determined by the saturated Fe magnetic moment and has a value of $f_0=22$ MHz in the Pr compound. In Eq. (20), the small contribution from the L^R_{3z} component which decreases as the ordered iron moment rotates is omitted. The decrease of the μSR frequency below T^{Pr}_N is roughly 2 MHz. Assuming a magnetic moment of approximately $1\mu_B$/Pr, a canting of $\sin\theta=0.42$ is obtained from Eq. (20). This estimation confirms indeed a strong tilting of the Fe moments to the z axis which was already concluded from Mössbauer spectroscopy experiments.[23] The respective magnetic structure is shown in Fig. 9(b). Note that in this model, the angle θ can achieve 90° if we suppose the Pr moments equal to $0.26\mu_B$/Pr. As mentioned above, the μSR signal would be exactly the same for another combined Fe-Pr magnetic structure with a nonzero noncollinear $L_{3x}\cos\theta+L_{1z}\sin\theta$ in the Fe and an L^{Pr}_{1y} order parameters in the Pr subsystem. We conclude that these two different magnetic structures are indistinguishable by μSR and Mössbauer studies.

Finally, we comment on other aspects of the Fe-R interactions. It is generally known that the Fe-R interaction plays a decisive role for the magnetic anisotropy of the Fe subsystem in Fe-R compounds. For instance, temperature-induced spin reorientation phase transitions, even far above of rare-earth magnetic order temperature, have been observed in rare-earth orthoferrites $ReFeO_3$ (Ref. 51) and in the $ReFe_{11}Ti$ compounds.[52] The temperature dependence of the Fe magnetic anisotropy is determined by competing contri-

butions from the Fe and *R* subsystems. In $ReFeO_3$ compounds, the *R* ordering is almost always accompanied by a Fe spin reorientation and the canting angles are relatively large due to a strong renormalization of the Fe magnetic anisotropy. In this sense, it would be surprising if the *R*FeAsO systems were an exception to this rule. Furthermore, it is clear that the large proposed Fe canting angles θ in Pr-ordered phase of PrFeAsO can be achieved by a renormalization of the Fe magnetic anisotropy but not solely by the direct Fe-Pr interaction mechanism (19).

Note that our μSR studies of *R*FeAsO with Sm, Pr, and Ce do not show temperature-induced spin reorientations of the iron magnetic structure in the Fe AFM phase. Spin reorientation starts at a temperature at which the anisotropy changes sign, i.e., it develops as a standard second-order phase transition. These have not been detected neither by change of the muon spin relaxation rate nor by other methods such as specific-heat or susceptibility studies. In the low-temperature range, the iron spin reorientation begins with the onset of the rare-earth magnetic order and therefore it can be masked by the latter.

IX. CONCLUSION

In conclusion, we presented a detailed study of the magnetic order and the interplay of the rare earth and iron magnetism in *R*FeAsO with *R*=La, Ce, Pr, and Sm, the magnetically ordered parent compounds of the recently discovered $RO_{1-x}F_xFeAs$ high-temperature superconductors. Using ZF μSR, the Néel temperatures, as well as the temperature dependence of the sublattice magnetizations, have been determined with high precision.

The second-order Fe magnetic phase transition is well separated from a structural transition which occurs 10–20 K above T_N. The muon site in the *R*FeAsO crystal structure has been obtained by electronic potential calculations involving a modified Thomas-Fermi approach. Using calculated dipole fields at the muon site, our μSR experiments indicate an antiferromagnetic commensurate order with the iron magnetic moments directed along the *a* axis above T_N^R. This is consistent with neutron-scattering results reported earlier.[43] The calculations show that the two types of iron order parameters with different translational symmetries that have been observed in *R*FeAsO compounds, i.e., with ($\mathbf{K}_{\mathrm{I}}$) and without ($\mathbf{K}_{\mathrm{II}}$) doubling of the magnetic primitive cell along the *c* direction, cause nearly the same field at the muon site and are therefore not distinguishable by μSR. Mössbauer spectroscopy[12,23] as well as μSR prove that the ordered Fe magnetic moment is approximately $0.4\mu_B$ and does not vary by more than 15% within the series *R*FeAsO with *R*=La, Ce, Pr, and Sm. This is in sharp contrast to published neutron results[43] where Fe magnetic moments of $0.36\mu_B$, $0.48\mu_B$, and $0.8\mu_B$ have been deduced for *R*=La, Pr, and Ce, respectively. In the neutron studies, the observed intensity in the magnetic Bragg peaks is solely attributed to an ordered Fe moment for temperatures larger than T_N^R. Here, we could show that a sizable magnetic moment of the *R* subsystem which is induced by the ordered Fe subsystem is already detectable far above T_N^R. Especially in CeFeAsO, this *R* magnetization is exceptionally large and amounts to approximately $0.3\mu_B$/Ce just above T_N^{Ce}. Since for symmetry reasons the Ce and Fe magnetic moments contribute to the same Bragg peaks, neglecting the Ce magnetization results in the strong overestimation of the Fe moment in the CeFeAsO system by neutron scattering.

Static magnetic ordering of the rare-earth moments has been observed for the *R*=Ce, Pr, and Sm compounds with transition temperatures of T_N^R=4.4(3), 11(1), and 4.66(5) K, respectively. Using available literature data of Mössbauer spectroscopy and neutron diffraction and the μSR data presented here, we propose combined *R* and Fe magnetic structures below T_N^R for all investigated compounds. For CeFeAsO, the μSR data are consistent with a noncollinear easy-plane AFM order of the Ce moments as concluded from neutron diffraction.[16] For SmFeAsO, several new μSR frequencies develop in the Sm ordered phase. To explain the μSR spectra, a minimal model of noncollinear Sm magnetic order is proposed. The additional μSR frequencies originate from different translational symmetries of the Sm and Fe order parameters. Analyzing structural features of *R*FeAsO, we argue that the noncollinear rare-earth magnetic order observed in Ce and Sm compounds arises due to a weak magnetic coupling of the adjacent *R* planes in the *R*-O-*R* layer. A weak coupling of the *R*-O-*R* layers is probably an inherent feature of all *R*FeAsO compounds. For PrFeAsO, we propose that the Pr moments order also with an easy-plane anisotropy. Our model therefore differs from the one determined by Zhao *et al.*[17] which implies an easy axis anisotropy in the Pr ordered phase. Only the model with easy-plane anisotropy is able to consistently describe the μSR and Mössbauer[23] as well as the neutron data.

Even though Fe spin reorientation phase transitions are frequently observed in *R*-Fe systems, e.g., in rare-earth orthoferrites $RFeO_3$ (Ref. 51) or $RFe_{11}Ti$,[52] we do not find such a transition in *R*FeAsO above T_N^R for *R*=Ce, Pr, and Sm. In the *R*-ordered phase, one can expect a strong influence of the rare-earth magnetic subsystem on the Fe ordering direction especially in the case when the iron and rare-earth order parameters have different symmetries. This is the case for collinear as well as noncollinear easy-plane AFM orders in the *R* subsystem. We suggest that this is the reason for the Fe spin reorientation developing below T_N^{Pr} as deduced from the μSR data on PrFeAsO.

Using symmetry arguments, we demonstrate the absence of a Heisenberg magnetic interaction between the Fe and the *R* subsystem in *R*FeAsO. Therefore, the apparent Fe-*R* interaction is realized by a non-Heisenberg anisotropic exchange. Our calculations additionally show that dipole-dipole interactions are much too weak to account for the observed couplings. We showed that in CeFeAsO, the Fe-Ce coupling is exceptionally large. This together with the large paramagnetic Ce magnetic moment explains the sizable Ce magnetization observed in our experiment in the Fe AFM ordered phase as well as the presence of a small component of Ce moment along the *c* axis in the Ce AFM ordered phase. For PrFeAsO, from a comparison of μSR, Mössbauer, and neutron-diffraction data, we derive a much weaker but noticeable Fe-Pr coupling constant which has opposite sign compared to the Fe-Ce coupling constant. For SmFeAsO, the

Fe-Sm coupling is very weak and the induced polarization of the Sm moments by the magnetically ordered Fe system is not measurable above T_N^{Sm}. Even though the lowest CEF levels in Sm and Ce are relatively similar, the low value of the Sm g factor reduces the induced Sm magnetic moment and therefore its contribution to the μSR frequency. The exceptionally strong coupling of the Ce to the Fe subsystem in CeFeAsO can also be understood from band-structure calculations. Only CeFeAsO possesses a considerable $3d$-$4f$ hybridization.[24–26] Additionally, the strong interaction of the two magnetic sublattices is in accordance with the observed strong electron correlation of the Ce $4f$ electrons and the heavy fermion behavior observed in the related phosphide CeOFeP.[27]

Finally, from our analysis, we can conclude that the magnetic R-Fe interaction is probably not crucial for the observed enhanced superconductivity in $RO_{1-x}F_xFeAs$ with magnetic $4f$ ions compared to $LaO_{1-x}F_xFeAs$, since only in CeFeAsO a strong R-Fe coupling is observed, while it is much weaker in the Pr and Sm compounds.

ACKNOWLEDGMENTS

We would like to thank M. Zhitomirsky, R. Moessner, I. M. Vitebsky, and N. M. Plakida for useful discussions. We thank M. Deutschmann, S. Müller-Litvanyi, R. Müller, and A. Köhler for experimental support in preparation and characterization of the samples. The work at TU Dresden has been supported by the DFG under Grant No. KL1086/8-1. Yu.G.P. acknowledges the support of the Ukrainian-Russian Grant No. 2008-8. The work at the IFW Dresden has been supported by the DFG through Grant No. FOR 538. Part of this work was performed at the Swiss Muon Source (Villigen, Switzerland).

APPENDIX

1. Magnitude and symmetry of dipole fields created by the iron and rare-earth subsystems at the A-type muon site

Below we provide the calculation of magnetic-dipole fields at the muon site A for different magnetic modes and different translational symmetries. The magnetic fields below are given in units of 10^{-1} T and basis functions L in units of μ_B. The coordinates of the muon site A are (0,1/4,0.41)

$$\begin{pmatrix} B_x(A) \\ B_y(A) \\ B_z(A) \end{pmatrix} = \begin{pmatrix} 0 & 0 & 0 \\ 0 & 0 & -2.56 \\ 0 & -2.56 & 0 \end{pmatrix} \begin{pmatrix} L_{1x}(\mathbf{K}_{\mathrm{I}}) \\ L_{1y}(\mathbf{K}_{\mathrm{I}}) \\ L_{1z}(\mathbf{K}_{\mathrm{I}}) \end{pmatrix} + \begin{pmatrix} 0 & 0 & 2.58 \\ 0 & 0 & 0 \\ 2.58 & 0 & 0 \end{pmatrix} \begin{pmatrix} L_{3x}(\mathbf{K}_{\mathrm{I}}) \\ L_{3y}(\mathbf{K}_{\mathrm{I}}) \\ L_{3z}(\mathbf{K}_{\mathrm{I}}) \end{pmatrix} + \begin{pmatrix} -0.79 & 0 & 0 \\ 0 & -0.66 & 0 \\ 0 & 0 & 1.45 \end{pmatrix} \begin{pmatrix} L^R_{1x}(\mathbf{K}_{\mathrm{I}}) \\ L^R_{1y}(\mathbf{K}_{\mathrm{I}}) \\ L^R_{1z}(\mathbf{K}_{\mathrm{I}}) \end{pmatrix} + \begin{pmatrix} -0.66 & 0 & 0 \\ 0 & -0.79 & 0 \\ 0 & 0 & 1.45 \end{pmatrix} \begin{pmatrix} L^R_{3x}(\mathbf{K}_{\mathrm{I}}) \\ L^R_{3y}(\mathbf{K}_{\mathrm{I}}) \\ L^R_{3z}(\mathbf{K}_{\mathrm{I}}) \end{pmatrix},$$

$$\begin{pmatrix} B_x(A) \\ B_y(A) \\ B_z(A) \end{pmatrix} = \begin{pmatrix} 0 & 0 & 0 \\ 0 & 0 & -2.55 \\ 0 & -2.55 & 0 \end{pmatrix} \begin{pmatrix} L_{1x}(\mathbf{K}_{\mathrm{II}}) \\ L_{1y}(\mathbf{K}_{\mathrm{II}}) \\ L_{1z}(\mathbf{K}_{\mathrm{II}}) \end{pmatrix} + \begin{pmatrix} 0 & 0 & 2.57 \\ 0 & 0 & 0 \\ 2.57 & 0 & 0 \end{pmatrix} \begin{pmatrix} L_{3x}(\mathbf{K}_{\mathrm{II}}) \\ L_{3y}(\mathbf{K}_{\mathrm{II}}) \\ L_{3z}(\mathbf{K}_{\mathrm{II}}) \end{pmatrix} + \begin{pmatrix} -0.89 & 0 & 0 \\ 0 & -0.59 & 0 \\ 0 & 0 & 1.48 \end{pmatrix} \begin{pmatrix} L^R_{1x}(\mathbf{K}_{\mathrm{II}}) \\ L^R_{1y}(\mathbf{K}_{\mathrm{II}}) \\ L^R_{1z}(\mathbf{K}_{\mathrm{II}}) \end{pmatrix} + \begin{pmatrix} -0.59 & 0 & 0 \\ 0 & -0.88 & 0 \\ 0 & 0 & 1.48 \end{pmatrix} \begin{pmatrix} L^R_{3x}(\mathbf{K}_{\mathrm{II}}) \\ L^R_{3y}(\mathbf{K}_{\mathrm{II}}) \\ L^R_{3z}(\mathbf{K}_{\mathrm{II}}) \end{pmatrix},$$

$$\begin{pmatrix} B_x(A) \\ B_y(A) \\ B_z(A) \end{pmatrix} = \begin{pmatrix} 2.16 & 0 & 0 \\ 0 & 2.12 & 0 \\ 0 & 0 & -4.28 \end{pmatrix} \begin{pmatrix} L_{1x}(\mathbf{K}_{\mathrm{III}}) \\ L_{1y}(\mathbf{K}_{\mathrm{III}}) \\ L_{1z}(\mathbf{K}_{\mathrm{III}}) \end{pmatrix} + \begin{pmatrix} 0 & -4.44 & 0 \\ -4.44 & 0 & 0 \\ 0 & 0 & 0 \end{pmatrix} \begin{pmatrix} L_{3x}(\mathbf{K}_{\mathrm{III}}) \\ L_{3y}(\mathbf{K}_{\mathrm{III}}) \\ L_{3z}(\mathbf{K}_{\mathrm{III}}) \end{pmatrix} + \begin{pmatrix} -0.40 & 0 & 0 \\ 0 & -0.40 & 0 \\ 0 & 0 & 0.80 \end{pmatrix} \begin{pmatrix} L^R_{1x}(\mathbf{K}_{\mathrm{III}}) \\ L^R_{1y}(\mathbf{K}_{\mathrm{III}}) \\ L^R_{1z}(\mathbf{K}_{\mathrm{III}}) \end{pmatrix} + \begin{pmatrix} -0.43 & 0 & 0 \\ 0 & -0.43 & 0 \\ 0 & 0 & 0.86 \end{pmatrix} \begin{pmatrix} L^R_{3x}(\mathbf{K}_{\mathrm{III}}) \\ L^R_{3y}(\mathbf{K}_{\mathrm{III}}) \\ L^R_{3z}(\mathbf{K}_{\mathrm{III}}) \end{pmatrix},$$

$$\begin{pmatrix} B_x(A) \\ B_y(A) \\ B_z(A) \end{pmatrix} = \begin{pmatrix} 1.59 & 0 & 0 \\ 0 & 1.55 & 0 \\ 0 & 0 & -3.15 \end{pmatrix} \begin{pmatrix} F_x(\mathbf{K}_0) \\ F_y(\mathbf{K}_0) \\ F_z(\mathbf{K}_0) \end{pmatrix} + \begin{pmatrix} 0 & -4.45 & 0 \\ -4.45 & 0 & 0 \\ 0 & 0 & 0 \end{pmatrix} \begin{pmatrix} L_{2x}(\mathbf{K}_0) \\ L_{2y}(\mathbf{K}_0) \\ L_{2z}(\mathbf{K}_0) \end{pmatrix} + \begin{pmatrix} -0.95 & 0 & 0 \\ 0 & -0.95 & 0 \\ 0 & 0 & 1.90 \end{pmatrix} \begin{pmatrix} F^R_x(\mathbf{K}_0) \\ F^R_y(\mathbf{K}_0) \\ F^R_z(\mathbf{K}_0) \end{pmatrix} + \begin{pmatrix} -0.44 & 0 & 0 \\ 0 & -0.44 & 0 \\ 0 & 0 & 0.88 \end{pmatrix} \begin{pmatrix} L^R_{2x}(\mathbf{K}_0) \\ L^R_{2y}(\mathbf{K}_0) \\ L^R_{2z}(\mathbf{K}_0) \end{pmatrix}.$$

2. Dipole fields created by the iron and rare-earth subsystems at the rare-earth site

Below we provide the calculation of magnetic-dipole fields at the rare-earth site for different magnetic modes and different translational symmetries. The magnetic fields below are given in units of 10^{-1} T and basis functions L in units of μ_B,

$$\begin{pmatrix} B_x(R) \\ B_y(R) \\ B_z(R) \end{pmatrix} = \begin{pmatrix} 0 & 0 & 0 \\ 0 & 0 & -0.52 \\ 0 & -0.52 & 0 \end{pmatrix} \begin{pmatrix} L_{1x}(\mathbf{K}_{\mathrm{I}}) \\ L_{1y}(\mathbf{K}_{\mathrm{I}}) \\ L_{1z}(\mathbf{K}_{\mathrm{I}}) \end{pmatrix} + \begin{pmatrix} 0 & 0 & 0.53 \\ 0 & 0 & 0 \\ 0.53 & 0 & 0 \end{pmatrix} \begin{pmatrix} L_{3x}(\mathbf{K}_{\mathrm{I}}) \\ L_{3y}(\mathbf{K}_{\mathrm{I}}) \\ L_{3z}(\mathbf{K}_{\mathrm{I}}) \end{pmatrix} + \begin{pmatrix} -0.30 & 0 & 0 \\ 0 & -1.29 & 0 \\ 0 & 0 & 1.59 \end{pmatrix} \begin{pmatrix} L^R_{1x}(\mathbf{K}_{\mathrm{I}}) \\ L^R_{1y}(\mathbf{K}_{\mathrm{I}}) \\ L^R_{1z}(\mathbf{K}_{\mathrm{I}}) \end{pmatrix} + \begin{pmatrix} -1.30 & 0 & 0 \\ 0 & -0.29 & 0 \\ 0 & 0 & 1.59 \end{pmatrix} \begin{pmatrix} L^R_{3x}(\mathbf{K}_{\mathrm{I}}) \\ L^R_{3y}(\mathbf{K}_{\mathrm{I}}) \\ L^R_{3z}(\mathbf{K}_{\mathrm{I}}) \end{pmatrix},$$

$$\begin{pmatrix} B_x(R) \\ B_y(R) \\ B_z(R) \end{pmatrix} = \begin{pmatrix} 0 & 0 & 0 \\ 0 & 0 & -0.45 \\ 0 & -0.45 & 0 \end{pmatrix} \begin{pmatrix} L_{1x}(\mathbf{K}_{\mathrm{II}}) \\ L_{1y}(\mathbf{K}_{\mathrm{II}}) \\ L_{1z}(\mathbf{K}_{\mathrm{II}}) \end{pmatrix} + \begin{pmatrix} 0 & 0 & 0.46 \\ 0 & 0 & 0 \\ 0.46 & 0 & 0 \end{pmatrix} \begin{pmatrix} L_{3x}(\mathbf{K}_{\mathrm{II}}) \\ L_{3y}(\mathbf{K}_{\mathrm{II}}) \\ L_{3z}(\mathbf{K}_{\mathrm{II}}) \end{pmatrix} + \begin{pmatrix} -1.32 & 0 & 0 \\ 0 & -0.28 & 0 \\ 0 & 0 & 1.60 \end{pmatrix} \begin{pmatrix} L^R_{1x}(\mathbf{K}_{\mathrm{II}}) \\ L^R_{1y}(\mathbf{K}_{\mathrm{II}}) \\ L^R_{1z}(\mathbf{K}_{\mathrm{II}}) \end{pmatrix} + \begin{pmatrix} -0.29 & 0 & 0 \\ 0 & -1.30 & 0 \\ 0 & 0 & 1.59 \end{pmatrix} \begin{pmatrix} L^R_{3x}(\mathbf{K}_{\mathrm{II}}) \\ L^R_{3y}(\mathbf{K}_{\mathrm{II}}) \\ L^R_{3z}(\mathbf{K}_{\mathrm{II}}) \end{pmatrix},$$

$$\begin{pmatrix} B_x(R) \\ B_y(R) \\ B_z(R) \end{pmatrix} = \begin{pmatrix} 0.03 & 0 & 0 \\ 0 & 0.03 & 0 \\ 0 & 0 & -0.06 \end{pmatrix} \begin{pmatrix} L_{1x}(\mathbf{K}_{\mathrm{III}}) \\ L_{1y}(\mathbf{K}_{\mathrm{III}}) \\ L_{1z}(\mathbf{K}_{\mathrm{III}}) \end{pmatrix} + \begin{pmatrix} 0 & -0.17 & 0 \\ -0.17 & 0 & 0 \\ 0 & 0 & 0 \end{pmatrix} \begin{pmatrix} L_{3x}(\mathbf{K}_{\mathrm{III}}) \\ L_{3y}(\mathbf{K}_{\mathrm{III}}) \\ L_{3z}(\mathbf{K}_{\mathrm{III}}) \end{pmatrix} + \begin{pmatrix} -0.12 & 0 & 0 \\ 0 & -0.13 & 0 \\ 0 & 0 & 0.25 \end{pmatrix} \begin{pmatrix} L^R_{1x}(\mathbf{K}_{\mathrm{III}}) \\ L^R_{1y}(\mathbf{K}_{\mathrm{III}}) \\ L^R_{1z}(\mathbf{K}_{\mathrm{III}}) \end{pmatrix} + \begin{pmatrix} 0.23 & 0 & 0 \\ 0 & 0.23 & 0 \\ 0 & 0 & -0.46 \end{pmatrix} \begin{pmatrix} L^R_{3x}(\mathbf{K}_{\mathrm{III}}) \\ L^R_{3y}(\mathbf{K}_{\mathrm{III}}) \\ L^R_{3z}(\mathbf{K}_{\mathrm{III}}) \end{pmatrix}.$$

*h.klauss@physik.tu-dresden.de

[1] Y. Kamihara, T. Watanabe, M. Hirano, and H. Hoson, J. Am. Chem. Soc. **130**, 3296 (2008).

[2] X. H. Chen, T. Wu, G. Wu, R. H. Liu, H. Chen, and D. F. Fang, Nature (London) **453**, 761 (2008).

[3] G. F. Chen, Z. Li, D. Wu, G. Li, W. Z. Hu, J. Dong, P. Zheng, J. L. Luo, and N. L. Wang, Phys. Rev. Lett. **100**, 247002 (2008).

[4] Z.-A. Ren, J. Yang, W. Lu, W. Yi, X.-L. Shen, Z.-C. Li, G.-C. Che, X.-L. Dong, L.-L. Sun, F. Zhou, and Z.-X. Zhao, Europhys. Lett. **82**, 57002 (2008).

[5] Z. A. Ren, J. Yang, W. Lu, W. Yi, G. C. Che, X. L. Dong, L. L. Sun, and Z. X. Zhao, Mater. Res. Innovations **12**, 105 (2008).

[6] P. Cheng, L. Fang, H. Yang, X. Y. Zhu, G. Mu, H. Q. Luo, Z. S. Wang, and H. H. Wen, Sci. China, Ser. G **51**, 719 (2008).

[7] D. J. Singh and M. H. Du, Phys. Rev. Lett. **100**, 237003 (2008).

[8] X. Zhu, H. Yang, L. Fang, G. Mu, and H.-H. Wen, Supercond. Sci. Technol. **21**, 105001 (2008).

[9] P. D. de Réotier and A. Yaouanc, J. Phys.: Condens. Matter **9**, 9113 (1997).

[10] C. Hess, A. Kondrat, A. Narduzzo, J. E. Hamann-Borrero, R. Klingeler, J. Werner, G. Behr, and B. Büchner, EPL **87**, 17005 (2009).

[11] S. A. J. Kimber, D. N. Argyriou, F. Yokaichiya, K. Habicht, S. Gerischer, T. Hansen, T. Chatterji, R. Klingeler, C. Hess, G. Behr, A. Kondrat, and B. Büchner, Phys. Rev. B **78**, 140503(R) (2008).

[12] H.-H. Klauss, H. Luetkens, R. Klingeler, C. Hess, F. J. Litterst, M. Kraken, M. M. Korshunov, I. Eremin, S.-L. Drechsler, R. Khasanov, A. Amato, J. Hamann-Borrero, N. Leps, A. Kondrat, G. Behr, J. Werner, and B. Büchner, Phys. Rev. Lett. **101**, 077005 (2008).

[13] C. de la Cruz, Q. Huang, J. W. Lynn, J. Li, W. Ratcliff II, J. L. Zarestky, H. A. Mook, G. F. Chen, J. L. Luo, N. L. Wang, and P. Dai, Nature (London) **453**, 899 (2008).

[14] H. Luetkens, H.-H. Klauss, M. Kraken, F. J. Litterst, T. Dellmann, R. Klingeler, C. Hess, R. Khasanov, A. Amato, C. Baines, M. Kosmala, O. J. Schumann, M. Braden, J. Hamann-Borrero, N. Leps, A. Kondrat, G. Behr, J. Werner, and B. Büchner, Nature Mater. **8**, 305 (2009).

[15] J. E. Hamann-Borrero *et al.* (unpublished).

[16] J. Zhao, Q. Huang, C. de la Cruz, S. Li, J. W. Lynn, Y. Chen, M. A. Green, G. F. Chen, G. Li, Z. Li, J. L. Luo, N. L. Wang, and P. Dai, Nature Mater. **7**, 953 (2008).

[17] J. Zhao, Q. Huang, C. de la Cruz, J. W. Lynn, M. D. Lumsden, Z. A. Ren, J. Yang, X. Shen, X. Dong, Z. Zhao, and P. Dai, Phys. Rev. B **78**, 132504 (2008).

[18] H. Luetkens, H.-H. Klauss, R. Khasanov, A. Amato, R. Klingeler, I. Hellmann, N. Leps, A. Kondrat, C. Hess, A. Köhler, G. Behr, J. Werner, and B. Büchner, Phys. Rev. Lett. **101**, 097009 (2008).
[19] R. S. Hayano, Y. J. Uemura, J. Imazato, N. Nishida, T. Yamazaki, and R. Kubo, Phys. Rev. B **20**, 850 (1979).
[20] C. Xu, M. Müller, and S. Sachdev, Phys. Rev. B **78**, 020501(R) (2008).
[21] C. Fang, H. Yao, W.-F. Tsai, J. P. Hu, and S. A. Kivelson, Phys. Rev. B **77**, 224509 (2008).
[22] Q. Huang, J. Zhao, J. W. Lynn, G. F. Chen, J. L. Luo, N. L. Wang, and P. Dai, Phys. Rev. B **78**, 054529 (2008).
[23] M. A. McGuire, R. P. Hermann, A. S. Sefat, B. C. Sales, R. Jin, D. Mandrus, F. Grandjean, and G. J. Long, New J. Phys. **11**, 025011 (2009).
[24] V. Vildosola, L. Pourovskii, R. Arita, S. Biermann, and A. Georges, Phys. Rev. B **78**, 064518 (2008).
[25] L. Pourovskii, V. Vildosola, S. Biermann, and A. Georges, Europhys. Lett. **84**, 37006 (2008).
[26] T. Miyake, L. Pourovskii, V. Vildosola, S. Biermann, and A. Georges, J. Phys. Soc. Jpn. **77**, Supplement C, 99 (2008).
[27] E. M. Brüning, C. Krellner, M. Baenitz, A. Jesche, F. Steglich, and C. Geibel, Phys. Rev. Lett. **101**, 117206 (2008).
[28] R. Khasanov, H. Luetkens, A. Amato, H.-H. Klauss, Z.-A. Ren, J. Yang, W. Lu, and Z.-X. Zhao, Phys. Rev. B **78**, 092506 (2008).
[29] Z.-A. Ren, G.-C. Che, X.-L. Dong, J. Yang, W. Lu, W. Yi, X.-L. Shen, Z.-C. Li, L.-L. Sun, F. Zhou, and Z.-X. Zhao, Europhys. Lett. **83**, 17002 (2008).
[30] I. M. Reznik, F. G. Vagizov, and R. Troc, Phys. Rev. B **51**, 3013 (1995).
[31] E. Holzschuh, A. B. Denison, W. Kündig, P. F. Meier, and B. D. Patterson, Phys. Rev. B **27**, 5294 (1983).
[32] H. Luetkens, M. Stingaciu, Yu. G. Pashkevich, K. Conder, E. Pomjakushina, A. A. Gusev, K. V. Lamonova, P. Lemmens, and H.-H. Klauss, Phys. Rev. Lett. **101**, 017601 (2008).
[33] Y. A. Izyumov, V. E. Naish, and R. P. Ozerov, *Neutron Diffraction of Magnetic Materials* (Consultants Bureau, Plenum Publishing Corporation, New York, 1991).
[34] O. V. Kovalev, in *Representations of the Crystallographic Space Groups*, edited by H. T. Stokes and D. M. Hatch (Gordon & Breach, Switzerland, 1993).
[35] E. F. Bertaut, Acta Crystallogr., Sect. A: Cryst. Phys., Diffr., Theor. Gen. Crystallogr. **24**, 217 (1968); J. Phys. (France) **32**, 462 (1971); J. Magn. Magn. Mater. **24**, 267 (1981).
[36] Yu. A. Izyumov and V. E. Naish, J. Magn. Magn. Mater. **12**, 239 (1979).
[37] H. Takenaka and D. J. Singh, Phys. Rev. B **78**, 052503 (2008).
[38] S. Chi, D. T. Adroja, T. Guidi, R. Bewley, S. Li, J. Zhao, J. W. Lynn, C. M. Brown, Y. Qiu, G. F. Chen, J. L. Lou, N. L. Wang, and P. Dai, Phys. Rev. Lett. **101**, 217002 (2008).
[39] J. P. Carlo, Y. J. Uemura, T. Goko, G. J. MacDougall, J. A. Rodriguez, W. Yu, G. M. Luke, P. Dai, N. Shannon, S. Miyasaka, S. Suzuki, S. Tajima, G. F. Chen, W. Z. Hu, J. L. Luo, and N. L. Wang, Phys. Rev. Lett. **102**, 087001 (2009).
[40] C. Bernhard, A. J. Drew, L. Schulz, V. K. Malik, M. Rössle, C. Niedermayer, T. Wolf, G. D. Varma, G. Mu, H.-H. Wen, H. Liu, G. Wu, and X. H. Chen, New J. Phys. **11**, 055050 (2009).
[41] A. J. Drew, Ch. Niedermayer, P. J. Baker, F. L. Pratt, S. J. Blundell, T. Lancaster, R. H. Liu, G. Wu, X. H. Chen, I. Watanabe, V. K. Malik, A. Dubroka, M. Rössle, K. W. Kim, C. Baines, and C. Bernhard, Nature Mater. **8**, 310 (2009).
[42] J. Mesot and A. Furrer, J. Supercond. **10**, 623 (1997).
[43] J. W. Lynn and P. Dai, Physica C **469**, 469 (2009).
[44] H. Luetkens *et al.* (unpublished).
[45] V. L. Sobolev, H. L. Huang, I. M. Vitebskii, A. N. Knigavko, and Yu. G. Pashkevich, Phys. Rev. B **48**, 3417 (1993).
[46] Yu. G. Pashkevich, V. L. Sobolev, S. A. Fedorov, and A. V. Eremenko, Phys. Rev. B **51**, 15898 (1995).
[47] Y. Qiu, W. Bao, Q. Huang, T. Yildirim, J. M. Simmons, M. A. Green, J. W. Lynn, Y. C. Gasparovic, J. Li, T. Wu, G. Wu, and X. H. Chen, Phys. Rev. Lett. **101**, 257002 (2008).
[48] H. M. Alyahyaei and R. A. Jishi, Phys. Rev. B **79**, 064516 (2009).
[49] C. de Graaf, I. de P. R. Moreira, F. Illas, O. Iglesias, and A. Labarta, Phys. Rev. B **66**, 014448 (2002).
[50] K. V. Lamonova *et al.* (unpublished).
[51] K. P. Belov, A. K. Zvezdin, A. M. Kadomtseva, and R. Z. Levitin, Sov. Phys. Usp. **19**, 574 (1976).
[52] C. Piquer, F. Grandjean, O. Isnard, and G. J. Long, J. Phys.: Condens. Matter **18**, 205 (2006).
[53] H.-H. Klauss, J. Phys.: Condens. Matter **16**, S4457 (2004).
[54] P. J. Baker, S. R. Giblin, F. L. Pratt, R. H. Liu, G. Wu, X. H. Chen, M. J. Pitcher, D. R. Parker, S. J. Clarke, and S. J. Blundell, New J. Phys. **11**, 025010 (2009).